Available online at www.sciencedirect.com

ScienceDirect

Underground Space 27 (2026) 194–215

www.keaipublishing.com/undsp

Research Paper

Macro-micro coupled analysis of synchronous grouting in coarse-grained strata: CFD–DEM insights into ground settlement control and fabric evolution

Chao Liu [a,b,*], Wei Chen [a], Delin Zhu [a], Junzuo He [a], Jie Cui [a,b], Xin Huang [c]

[a] *School of Civil Engineering and Transportation, Guangzhou University, Guangzhou 510006, China*
[b] *Guangdong Engineering Research Center for Underground Infrastructural Protection in Coastal Clay Area, Guangzhou University, Guangzhou 510006, China*
[c] *Department of Geotechnical Engineering, College of Civil Engineering, Tongji University, Shanghai 200092, China*

Received 27 April 2025; received in revised form 14 October 2025; accepted 28 October 2025
Available online 7 January 2026

Abstract

This study investigates the macro- and micro-mechanism of synchronous tail grouting in ground surface settlement (GSS) control of coarse-grained strata through a computational fluid dynamics-discrete element method (CFD–DEM) coupled model, focusing on two grouting port configurations (Type I: upper-lower symmetrical layout; Type II: lateral staggered distribution) in six-grouting-port shield machines. Analyzing particle contact characteristics and force chain evolution patterns, the connection between particle-scale behavior and macroscale GSS during grouting is elucidated. Key findings demonstrate that grouting duration is the primary factor for GSS development. Grout injection disrupted the particle contacts and force-chain networks above the tunnel center, weakening natural arching and redistributing interparticle forces. The central axis of the soil-arching effect exhibited a strong linear correlation with the spatial position of the uppermost grouting port. The soil located 0.25D–0.5D (where D represents the tunnel diameter) from the tunnel centerline horizontally, exhibited heightened sensitivity to grouting, with a low fabric anisotropy (α) and oscillating principal direction (β) sharply between 0° and 180°, reflecting pronounced displacement and isotropy. This study provides theoretical support for intelligent shield machine selection and grouting strategy optimization in geotechnical engineering, with significant implications for soil displacement control in complex strata.

Keywords: Synchronous grouting; CFD–DEM; Coarse-grained ground; Microstructure; Fabric evolution

1 Introduction

The rapid expansion of urban infrastructure has driven the widespread adoption of super-large-diameter shield tunnels (>14 m) in recent years (Su et al., 2024; Zeng et al., 2023; W. Zhang et al., 2022). A critical challenge in shield tunneling arises from the annular tail-void formed between the surrounding soil and tunnel lining due to geometric discrepancies between the shield machine and segments (Zhao et al., 2019). This void poses substantial risks, including soil collapse, ground surface settlement (GSS), and segment buoyancy. Synchronous grouting, a process designed to fill the tail-void with cementitious materials, serves as a primary mitigation measure. Besides GSS control (Wang et al., 2019), it enhances tunnel waterproofing (Wang et al., 2022) and optimizes the lining stress states (Liang et al., 2020; J. Liu et al., 2021). However, grouting efficacy depends on interdependent factors spanning grouting parameters, e.g., grout pressure (Liu et al., 2019), grout rheology (Liang et al., 2022; Todaro & Pace, 2022), geological conditions (Ye et al., 2019), and

---

[*] Corresponding author at: School of Civil Engineering and Transportation, Guangzhou University, Guangzhou 510006, China.
E-mail address: chaoliu@gzhu.edu.cn (C. Liu).

Peer review under the responsibility of Tongji University

https://doi.org/10.1016/j.undsp.2025.10.005

operational variables such as grouting-port configuration and shield advance rate (Zhang et al., 2015). The opaque nature of soil-grout interactions hinders mechanistic understanding, necessitating advanced methodologies to unravel this multiscale fluid–solid coupling process.

Early research prioritized theoretical models to characterize grout propagation modes under idealized assumptions. Analytical frameworks addressed radial filling (Zou & Zuo, 2017), permeation-compaction-fracturing transitions (Ye et al., 2020), and time-dependent pressure distributions incorporating grout viscosity and soil porosity (Liu et al., 2020; Ye et al., 2019). Although cost-effective, such models oversimplify complex soil-fluid interactions, limiting their applicability to field conditions. Experimental approaches subsequently provided empirical insights. Scaled tests revealed grouting port quantity and layout effects (Ding et al., 2019; Zhang et al., 2015), linking pressure and grout-type variations to GSS magnitudes (Zhao et al., 2019). Recent experiments in coarse-grained and soft soils highlight contrasting grout distribution patterns: uneven crown filling in granular strata versus uniform void occupation in cohesive soils (C. Liu et al., 2024b; F. Liu et al., 2024). However, the scalability constraints in physical tests and high costs restrict their capacity to replicate in situ complexities.

Numerical simulations offer a versatile alternative, yet conventional finite element methods (FEM) often neglect critical microscale interactions by approximating grout layers as static annular loads (Kasper & Meschke, 2006; C. Liu et al., 2021; D. Zhang et al., 2022). Advanced computational techniques, including the coupled discrete element method (DEM) and computational fluid dynamics (CFD) models, have begun bridging this gap. For instance, CFD analyses have elucidated longitudinal grout spreading (Li et al., 2021), whereas DEM–FDM hybrids have been used to simulate grout flow from ports to voids (Yan et al., 2024). Notably, C. Liu et al. (2024a) employed CFD–DEM to investigate the soil-grout interaction in coarse-grained ground, providing a more comprehensive understanding of the process. Despite the progress, existing studies predominantly focus on macroscopic behavior, overlooking the micromechanical mechanisms governing particle-scale force transmission and fabric evolution (Bokkisa et al., 2023; Irani et al., 2024; Zhang et al., 2023). This gap is particularly acute for large-diameter shields employing six or more grouting ports, which remain underexplored in terms of optimized port arrangements.

In this study, the CFD–DEM method was used to establish numerical models for simulating synchronous tail-grouting during shield tunneling in sandy cobble strata, a complex process involving particle–fluid interaction. Compared to the model of Liu et al. (2024a), two different grouting port distributions (Types I and II, both with six ports) were considered. The specific content of this study is as follows. Numerical models with different grouting-port distributions were established based on the geometry of a scaled model test (Liu et al., 2024b). The numerical models were validated through settlement trough curves predicted by the Peck formula based on scaled model tests. The relationship between different grouting opening distributions, soil displacement, and grout spreading modes, was examined. The microscopic fabric of particle contacts was analyzed to investigate the evolution of soil stress and its influence on soil mechanical behavior. The study revealed the microscopic mechanisms of particle interactions and explained the causes of macroscopic phenomena during synchronous grouting from a microscopic perspective.

2 Methodology

The CFD–DEM method was first proposed by Goniva et al. (2012) and Kloss et al. (2012). In this approach, the fluid phase is simulated using the open-source CFD software package OpenFOAM, and the soil particles are simulated using the open-source DEM software package LIGGGHTS. The cfdemSolverMultiphase solver, developed by Vångö et al. (2018) based on the OpenFOAM solver multiphaseInterFoam and LIGGGHTS code is employed in this study. The corresponding governing equations of motion are as follows.

2.1 Governing equations for DEM

In the DEM method (Cundall & Strack, 1979), the motion of spherical particles is tracked in the Lagrangian framework according to Newton's laws of motion. Owing to the high computational cost associated with modeling polygonal or non-spherical particles and simulating particle crushing, these features were not incorporated into the study. For each particle in the simulation system, the governing equations of motion are as follows:

$$m_{\mathrm{p}i}\frac{\mathrm{d}\boldsymbol{u}_{\mathrm{p}i}}{\mathrm{d}t}=\sum_{j=1}^{n_{\mathrm{c}}}\boldsymbol{F}_{\mathrm{p}ij}^{\mathrm{c}}+\boldsymbol{F}_{\mathrm{p}i}^{\mathrm{g}}+\boldsymbol{F}_{\mathrm{p}i}^{\sigma}+\boldsymbol{F}_{\mathrm{p}i}^{\mathrm{f}}, \tag{1}$$

$$I_{\mathrm{p}i}\frac{\mathrm{d}\boldsymbol{\omega}_{\mathrm{p}i}}{\mathrm{d}t}=\sum_{j=1}^{n_{\mathrm{c}}}\boldsymbol{M}_{\mathrm{p}ij}, \tag{2}$$

where $m_{\mathrm{p}i}$ is the mass of particle i; $\boldsymbol{u}_{\mathrm{p}i}$ is the translational motion of particle i; n_{c} is the total number of contacts for particle i; $\boldsymbol{F}_{\mathrm{p}ij}^{\mathrm{c}}$ is the contact force between particles i and j; $\boldsymbol{F}_{\mathrm{p}i}^{\mathrm{g}}$ is the gravitational force over particle i, $\boldsymbol{F}_{\mathrm{p}i}^{\sigma}=V_{\mathrm{p}i}\boldsymbol{F}_{\sigma}$ is the surface tension force of particle i, $V_{\mathrm{p}i}$ is the volume of particle i, $\boldsymbol{F}_{\sigma}$ is the surface tension force, $\boldsymbol{F}_{\mathrm{p}i}^{\mathrm{f}}$ is the particle–fluid interaction force of particle i, $I_{\mathrm{p}i}$ is the moment of inertia of particle i, $\boldsymbol{\omega}_{\mathrm{p}i}$ is the angular velocity of particle i; $\boldsymbol{M}_{\mathrm{p}ij}$ is the moment acting on particle i due to contact with particle j.

2.2 Governing equations of CFD

In the finite volume method (FVM) (Anderson & Jackson, 1967), the fluid phase is discretized into control volume, and used to solve the mass continuity and Navier–Stokes equations, as follows:

$$\frac{\partial \phi_{\mathrm{f}}}{\partial t} + \nabla \cdot (\phi_{\mathrm{f}} \boldsymbol{u}_{\mathrm{f}}) = 0, \tag{3}$$

$$\frac{\partial \phi_{\mathrm{f}} \rho_{\mathrm{f}} \boldsymbol{u}_{\mathrm{f}}}{\partial t} + \nabla(\phi_{\mathrm{f}} \rho_{\mathrm{f}} \boldsymbol{u}_{\mathrm{f}} \boldsymbol{u}_{\mathrm{f}}) = -\phi_{\mathrm{f}} \nabla p^{*} - \phi_{\mathrm{f}} g \cdot x \nabla \rho_{\mathrm{f}} + \phi_{\mathrm{f}} \nabla \cdot \tau + \phi_{\mathrm{f}} \boldsymbol{F}_{\sigma} + \boldsymbol{F}_{\text{p-f}}, \tag{4}$$

where ϕ_{f} is the volume fraction of the fluid in a fluid cell; $\boldsymbol{u}_{\mathrm{f}}$ is the fluid velocity, ρ_{f} is the weighted density of the mixed fluid; p^{*} is the dynamic pressure; $p^{*} = p - \rho_{f} \boldsymbol{g} \cdot \boldsymbol{x}$, where p is the fluid pressure and $\boldsymbol{g}$ is the acceleration of gravity, $\boldsymbol{x}$ is the coordinate vector; $\boldsymbol{\tau}$ is the viscous stress tensor of the fluid; $\boldsymbol{F}_{\sigma}$ is the surface tension force; and $\boldsymbol{F}_{\text{p-f}}$ is the fluid-particle interaction force. The direct numerical simulation (DNS) method is employed to simulate grout flow behavior. DNS directly solves the Navier-Stokes equations, allowing precise resolution of fluid motion without relying on turbulence models or empirical approximations.

2.3 Fluid and particle interaction forces

In the cfdemSolverMultiphase solver, the primary fluid-particle interaction force models (Zhu et al., 2007) considered include the pressure gradient force ($\boldsymbol{F}_{\mathrm{p}i}^{\nabla p}$), viscous force ($\boldsymbol{F}_{\mathrm{p}i}^{\nabla \tau}$), and drag force ($\boldsymbol{F}_{\mathrm{p}i}^{\mathrm{drag}}$). Other fluid-particle interaction force models, such as lubrication and added-mass forces, are ignored. Therefore, the total fluid-particle interaction force is calculated as follows:

$$\boldsymbol{F}_{\mathrm{p}i}^{\mathrm{f}} = \boldsymbol{F}_{\mathrm{p}i}^{\nabla p} + \boldsymbol{F}_{\mathrm{p}i}^{\nabla \cdot \tau} + \boldsymbol{F}_{\mathrm{p}i}^{\mathrm{drag}}, \tag{5}$$

$$\boldsymbol{F}_{\mathrm{p}i}^{\nabla p} = -V_{\mathrm{p}i} \nabla p, \tag{6}$$

$$\boldsymbol{F}_{\mathrm{p}i}^{\nabla \cdot \tau} = V_{\mathrm{p}i} \nabla \cdot \boldsymbol{\tau}, \tag{7}$$

$$\boldsymbol{F}_{\mathrm{p}i}^{\mathrm{drag}} = \frac{V_{\mathrm{p}i} \beta}{\phi_{\mathrm{p}}} \left(\boldsymbol{u}_{\mathrm{f}} - \boldsymbol{u}_{\mathrm{p}i} \right). \tag{8}$$

The pressure gradient and viscous forces were calculated based on the pressure gradient and viscous shear stress, respectively. The drag force was computed using the drag model proposed by Koch and Hill (2001), where ϕ_{p} is the solid volume fraction and β is the interphase momentum exchange coefficient, which can be expressed as

$$\beta = \frac{18 \mu_{\mathrm{f}} \phi_{\mathrm{f}}^{2} \phi_{\mathrm{p}}}{d_{\mathrm{p}i}^{2}} \left(F_{0}\left(\phi_{\mathrm{p}}\right) + \frac{1}{2} F_{3}(\phi_{\mathrm{p}}) Re_{\mathrm{p}} \right), \tag{9}$$

$$\mathrm{Re}_{\mathrm{p}} = \frac{\rho_{\mathrm{f}} \phi_{\mathrm{f}} d_{\mathrm{p}i} \left| \boldsymbol{u}_{\mathrm{f}} - \boldsymbol{u}_{\mathrm{p}i} \right|}{\mu_{\mathrm{f}}}, \tag{10}$$

where μ_{f} is the fluid dynamic viscosity; $d_{\mathrm{p}i}$ is the particle diameter; Re_{p} is the Reynolds number; $F_{0}\left(\phi_{\mathrm{p}}\right)$ and $F_{3}(\phi_{\mathrm{p}})$ are dimensionless parameters. These parameters are calculated using the following formulae:

$$F_{0}\left(\phi_{\mathrm{p}}\right) = \begin{cases} \dfrac{1+3\sqrt{\frac{\phi_{\mathrm{p}}}{2}}+\frac{135}{64}\phi_{\mathrm{p}}\ln\phi_{\mathrm{p}}+16.14\phi_{\mathrm{p}}}{1+0.681\phi_{\mathrm{p}}-8.48{\phi_{\mathrm{p}}}^{2}+8.16{\phi_{\mathrm{p}}}^{3}}, \phi_{\mathrm{p}} < 0.4, \\ \dfrac{10\phi_{\mathrm{p}}}{(1-\phi_{\mathrm{p}})^{3}}, \phi_{\mathrm{p}} > 0.4, \end{cases} \tag{11}$$

$$F_{3}(\phi_{\mathrm{p}}) = 0.0673 + 0.212\phi_{\mathrm{p}} + \frac{0.0232}{(1-\phi_{\mathrm{p}})^{5}}. \tag{12}$$

The computational process is divided into two independent modules: CFD and DEM, with information exchange at specified time intervals. The coupled CFD–DEM calculation process is illustrated in Fig. 1.

3 Numerical model setup and validation

3.1 Model description and setup

C. Liu et al. (2024b) performed 1g scaled model tests to characterize synchronous grout propagation behavior in sandy cobble strata during shield tunneling, with the experimental configuration schematically illustrated in Fig. 2. Building upon these experimental foundations, this study developed a CFD–DEM framework to numerically replicate the grouting process in analogous granular soils. The CFD module resolves grout-air multiphase flow dynamics, whereas the DEM module explicitly models the discrete sandy cobble matrix and its micromechanical interactions.

Engineering practice and scaled model tests consistently demonstrate a temporal lag between shield advancement and tail synchronous grouting activation, wherein grout injection commences following a short machine progression. To streamline numerical analysis, this study approximates the grouting process as porous medium infiltration. Building on the scaled test platform by C. Liu et al. (2024b), a two-phase CFD–DEM framework was implemented, adopting x-y plane symmetry through half-structure modeling with the geometry parameters detailed in Fig. 3. The model dimensions in the x and y directions were consistent with the scaled model test to preserve geometric similarity. The numerical domain measures 600 mm (x) × 1600 mm (y) × 50 mm (z), featuring a centrally positioned 400 mm diameter tunnel located 600 mm above the base and 1000 mm below the model surface. The numerical model followed a similarity ratio of 15, consistent with the scaled test. The z-direction thickness was set to 50 mm, equivalent to approximately half the length of a segment ring in the prototype. Although the model thickness was limited by computational constraints, it adequately

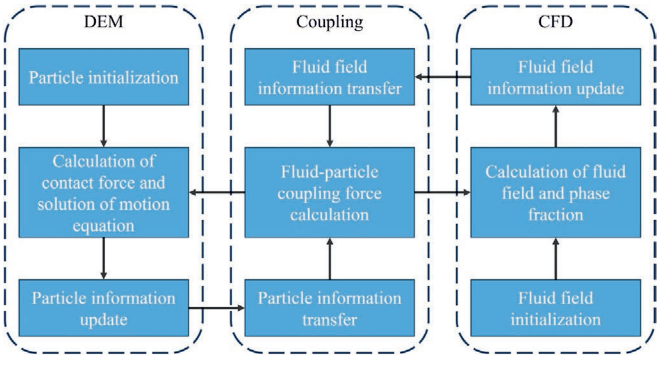

Fig. 1. Flowchart of CFD–DEM coupling calculation.

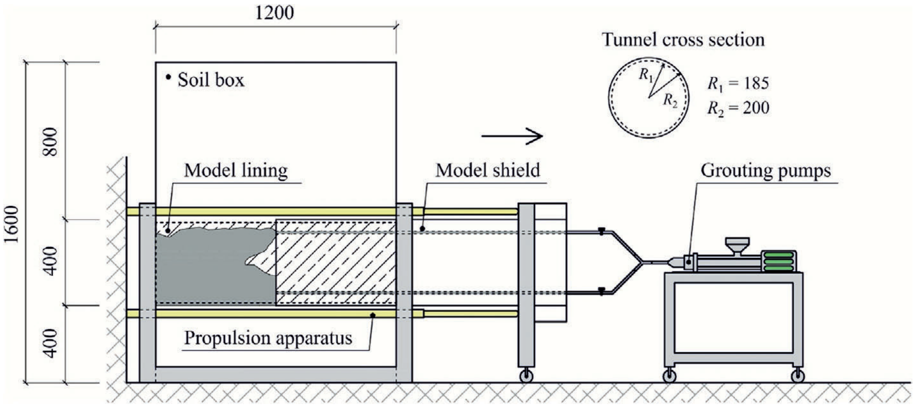

Fig. 2. Schematic diagram of the grouting model test (C. Liu et al., 2024b). (Unit: mm)

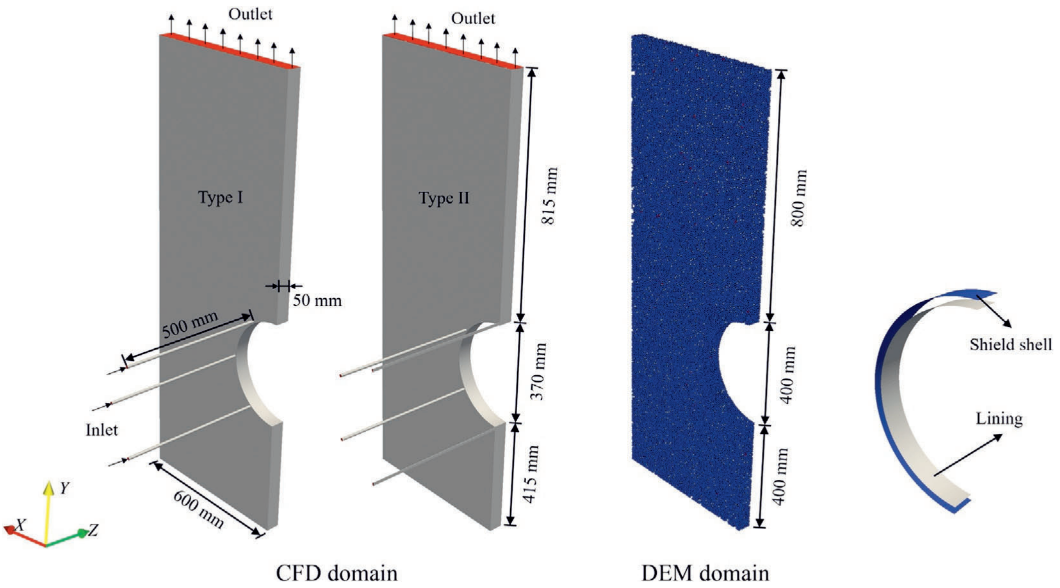

Fig. 3. Overview of the grouting model in the CFD and DEM domains.

captured circumferential grout-spread behavior. Grouting pipes (10 mm diameter × 500 mm length) were arranged according to the six-port configurations, with the Type I and II distributions illustrated in Fig. 4. For Type II, top/bottom pipes were modeled as half-sections owing to symmetry plane alignment.

Initial CFD conditions defined the primary domain as air (with a gas volume fraction of 1.0) and pipe interiors as grout (with a liquid volume fraction of 1.0), both phases were treated as Newtonian fluids with constant viscosity. Grout transport properties obtained from the previous model tests (C. Liu et al., 2024b) are listed in Table 1. The grout behavior was simulated using the Newtonian fluid model based on the following two considerations:

(1) The grout used in the scaled model test had a water-cement ratio (m_W/m_C) of 1.95. According to the study by Ruan (2005), the rheological behavior of grout varies with the m_W/m_C and does not conform to a single flow type. Specifically, grout with $m_W/m_C = 0.5–0.7$ exhibits power-law fluid behavior, with $m_W/m_C = 0.8–1.0$ corresponds to Bingham fluid behavior, and $m_W/m_C = 2.0–10.0$ approximating Newtonian fluid behavior. A m_W/m_C of 1.0 represents the transition point between Bingham and

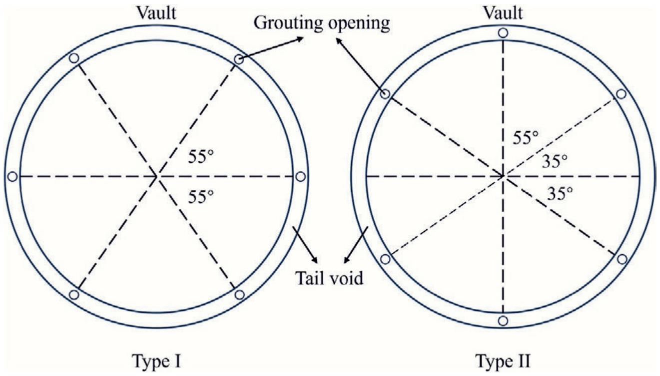

Fig. 4. Distribution of grouting ports: Types I and II.

Table 1
Numerical parameters in the simulation.

Simulation modules	Parameter	Value or type
Grout	Fluid type	Newtonian
	Density	1769 kg/m^3
	Kinematic viscosity	5.5×10^{-5} m/s^2
	Dynamic viscosity	0.097 Paṡ
Particle	Density	2200 kg/m^3
	Contact model	Hertz
	Young's modulus	20 GPa
	Poisson's ratio	0.3
	Coefficient of restitution	0.2
	Coefficient of friction	0.5
Coupling settings	CFD timestep	1.25×10^{-5} s
	DEM timestep	2.5×10^{-7} s
	Coupling interval	50
	Void fraction model	Divided
	Force models	Gradient pressure force Viscous force Koch and Hill drag force Surface tension force

Newtonian fluids. Therefore, given the relatively high m_W/m_C used in this study, it was reasonable to simplify the grout as a Newtonian fluid. Moreover, some practical engineering applications employ Newtonian fluid for grout; (2) Under the current numerical framework, directly implementing a Bingham model presents technical challenges and may result in non-convergence or interruptions in the simulation process. It should be noted that actual grout comprises many fine particles. However, these were not explicitly simulated in the current simulations owing to limitations in computational resources. Boundary conditions comprised: Inlet (fluid entry), Outlet (fluid exit), and Wall (all other surfaces), as annotated in Fig. 3. In actual construction, the next excavation step is usually carried out after the grout has preliminarily solidified. Consequently, the backward spread of newly injected grout is impeded by the already solidified grout. Moreover, structures such as the shield tail and tail brushes restrict the grout from flowing forward (i.e., towards the tunnel face). As a result, longitudinal spread of grout beyond the filling zone is not prominent in actual engineering scenarios. In this study, the focus was mainly on the circumferential spread of grout, and a systematic analysis of its longitudinal diffusion has not yet been conducted. Therefore, the numerical model restricted grout flow in the longitudinal direction, with only the top boundary serving as the fluid outlet. A constant flow rate was set at the inlet boundary, specified using the flowRateInletVelocity keyword. The inlet flow rate was determined based on scaled model tests and calculated using the following formula:

$$Q = \frac{\alpha_{\mathrm{GVR}} \cdot \pi (R_s^2 - r_s^2) \cdot v}{2 \times 3 \times z_s}, \tag{13}$$

where α_{GVR} is the grout-volume ratio (GVR), set at 200%; R_s is the radius of the shield-shell (200 mm); r_s is the radius of the segment lining (185 mm); v is the tunnel advance rate (15 mm/s); z_s is the axial thickness (50 mm); and Q is the grout flow rate per grouting opening. Based on this equation, the inlet flow rate for a single grout opening was calculated as 0.91×10^{-4} m^3/s. For computational efficiency, this value was rounded to 1×10^{-4} m^3/s in the numerical simulations, achieving 200%GVR within 3 s. Because this study primarily investigated the initial stage of grout injection, the time-dependent stiffening effect of the grout was not included in the simulation. Temporal resolution was governed by computational stability via the Rayleigh criterion (Burns et al., 2019).

The geometric configuration of the DEM model is depicted in Fig. 3. Consistent with the CFD approach, a half-structure model was implemented to leverage symmetry. The tunnel, with a diameter of 400 mm, was centered 600 mm above the model base and 1000 mm below the model surface, yielding a burial depth of 800 mm (equivalent to twice the tunnel diameter, 2*D*). Particle size distribution and mechanical parameters were adopted from the calibration by C. Liu et al. (2024a), as detailed in Fig. 5 and Table 1. During DEM initialization, spherical particles were generated within a predefined domain, and mechanical equilibrium was attained following gravitational settling. After removing extraneous particles outside the target region, the final simulation comprised 312 412 particles. As shown in Fig. 3, particle motion in the initial phase was restricted by a semi-circular shield-shell boundary (400 mm diameter), representing the mechanical support provided by the shield machine. Subsequent separation of the shield and lining segments was simulated by deactivating the shell boundary and introducing a 370 mm diameter lining boundary, consistent with the scaled test dimensions (C. Liu et al., 2024b). Key coupling parameters are summarized in Table 1.

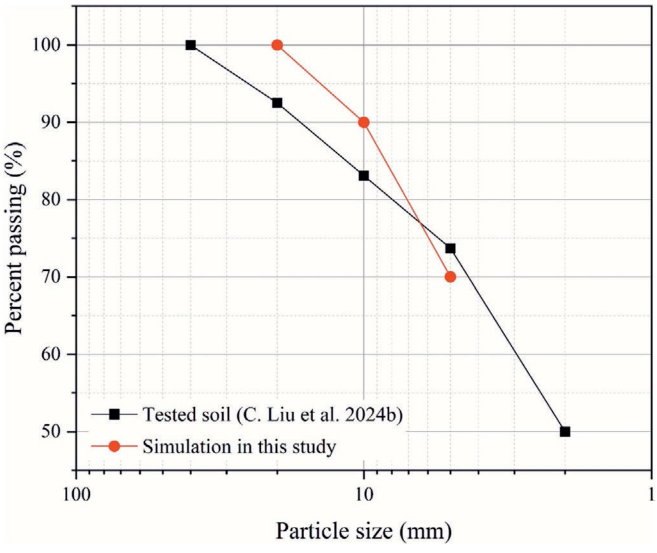

Fig. 5. Cumulative particle-size plot of the particles.

3.2 Boundary validation

To evaluate the validity of the symmetry assumption, a numerical simulation was conducted for the full-domain of lateral staggered layouts. A systematic comparison was made between half- and full-domain models in terms of grout spreading modes and GSS. Figure 6(a) presents the volume fraction distribution of grout, where the volume fraction is a dimensionless parameter ranging from 0 to 1. A value of 1 indicates that a fluid cell is fully occupied by grout, whereas a value of 0 denotes a cell entirely filled with air. In the full-domain model, the circumferential spread angles of the grout at the top were 32.6° on the left and 30.5° on the right, with a maximum radial spread distance of 79.8 mm. The corresponding values in the half-domain model were 32.6° and 70.8 mm, respectively, indicating close agreement. At the bottom, the maximum radial spread distance was 97.9 mm in the full-domain model and 88.8 mm in the half-domain model, resulting in a relative error of 9.3%, which is considered acceptable.

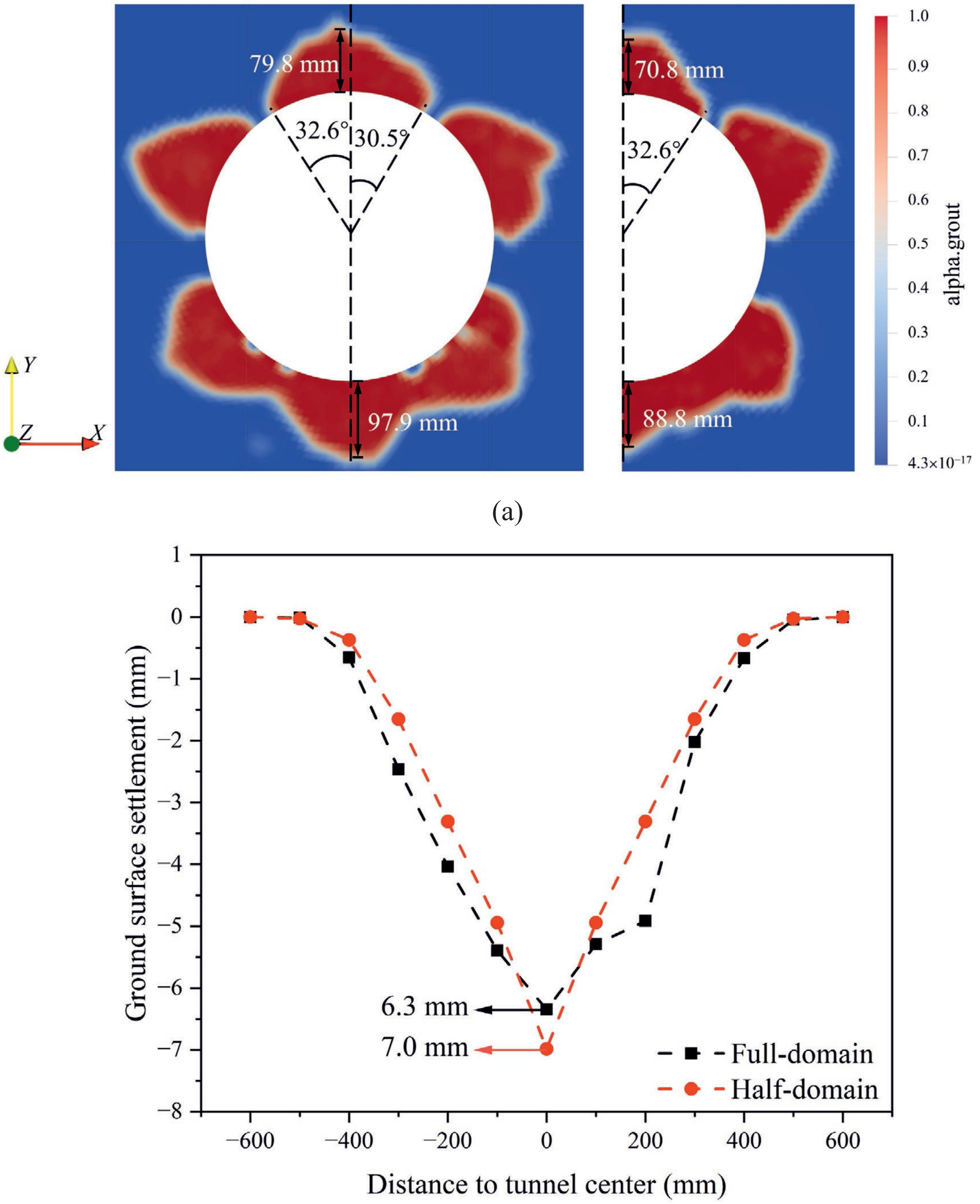

(a)

(b)

Fig. 6. Validation of the symmetry assumption. (a) Grout-spreading modes, and (b) GSS.

Owing to the intersection of grout flowing from adjacent grouting openings at the bottom, the circumferential spread angle in this region was excluded from the comparisons. For GSS, the maximum value was 6.3 mm in the full-domain model and 7.0 mm in the half-domain model, showing a difference of 11.1%, which was also deemed acceptable. In conclusion, the variations in grout spreading modes and GSS between the half- and full-domain models remained within acceptable limits, thereby validating the applicability of the symmetry assumption in the numerical model.

3.3 Model validation

In shield tunneling engineering, GSS is a ubiquitous concern, representing the spatial–temporal evolution of subsurface deformation caused by stress redistribution, soil arching effects, and void formation during excavation. As a direct indicator of geo-mechanical disturbance, GSS serves as a critical metric for evaluating the construction-induced impacts on surrounding strata. Peck (1969) pioneered a semi-empirical framework for predicting transverse settlement troughs in homogeneous soils, derived from field observations and soil mechanics principles. The model defines the vertical displacement $S(x)$ at a transverse distance x from the tunnel centerline as

$$S(x) = S_{\max}\exp\left(-\frac{x^2}{2i^2}\right), \tag{14}$$

$$S_{\max} = \frac{V_{\mathrm{S}}}{i\sqrt{2\pi}}, \tag{15}$$

$$V_{\mathrm{S}} = V_{\mathrm{L}}\pi R^2, \tag{16}$$

$$i = kz, \tag{17}$$

where $S(x)$ is the GSS (mm); $S_{\max}$ is the maximum vertical displacement of the settlement trough (mm); x is the distance to the tunnel centerline (m); V_{S} is the volume of soil loss per unit length (m^3/m); R is the tunnel radius (m); and V_{L} is the volume loss ratio, defined as the ratio of the settlement trough volume to tunnel volume. The V_{L} is a dimensionless parameter primarily influenced by engineering geological conditions, tunneling methods, and technical levels. The parameter i is the horizontal distance from the tunnel center to the inflection point of the settlement trough, commonly referred to as the width of the settlement trough, and is measured in meters. Empirical studies (O'reilly & New, 1982) have demonstrated a simple linear relationship between i and the tunnel axis burial depth z (m). The coefficient k, known as the settlement trough width coefficient, is a dimensionless parameter that determines the shape of the settlement trough curve (e.g., wide and shallow, or narrow and deep) and is largely dependent on soil properties. Therefore, V_{L} and k are two critical parameters in GSS prediction.

To thoroughly investigate the development of GSS and soil structure, the non-grouting condition ($\alpha_{\mathrm{GVR}} = 0$) was set as the benchmark for the comparative analysis in this study. As indicated in Table 2, results from the model test (C. Liu et al., 2024b) demonstrated that the settlement trough width coefficients (k) derived from experiments under varying burial depth ratios ($C/D = 1.0$, 1.5, and 2.0; where C is the thickness of tunnel covering soil; D is the tunnel diameter) were 0.265, 0.198, and 0.118, respectively, at a 200%GVR. The average value of k was 0.194 (denoted as $\bar{k}$), which was employed to characterize the mechanical behavior of the sandy cobble stratum. Numerical simulations further revealed that the V_{L} for Type I and Type II under the same GVR were 2.0% and 2.2%, respectively, whereas the V_{L} for the non-grouting case was 1.0%. By integrating $\bar{k}$ from the model test with the V_{L} calculated by numerical models, settlement prediction curves were established (Fig. 7). The results demonstrated that the GSS obtained from numerical simulations closely aligns with the prediction curve generated by the Peck formula, thereby validating the reliability of the proposed numerical approach. However, the GSS at the tunnel center for Type II exhibited a notable deviation from the maximum value of the predicted settlement trough. This discrepancy is attributed to the influence of an additional grouting opening at the tunnel crown, in contrast to the conventional four-opening grouting configuration (C. Liu et al., 2024b). Notably, V_{L} was influenced not only by soil properties but also by various factors such as GVR, tunnel depth, and grouting pressure. The V_{L} obtained from the scaled model test was 2.5%, which is slightly higher than the values obtained from the numerical simulations. This discrepancy is primarily attributed to differences in grouting configurations: the numerical model employed a six-hole arrangement, whereas the scaled model test used a four-hole configuration. These findings suggest that under otherwise identical conditions, six-hole grouting is more effective than four-hole grouting in mitigating GSS. Moreover, the study revealed a phenomenon that contradicts conventional engineering understanding: the GSS under grouting conditions was significantly greater than that under non-grouting conditions. Although this finding appears counterintuitive, it aligns with the conclusions of C. Liu et al. (2024a, 2024b), who reported a similar trend in numerical simulations and scaled model tests, indicating a positive correlation between GVR and GSS in coarse-grained strata. This consistency further substantiates the validity of the present model. The underlying mechanism stems from the distinctive mechanical behavior of the stratum. Unlike the soft clay typically modeled as a continuous

Table 2
Coefficient k calculated from the model test results (C. Liu et al., 2024b).

Case	C/D	GVR (%)	i (mm)	z (mm)	k	$\bar{k}$
1	1	200	159	600	0.265	0.194
2	1.5	200	158	800	0.198	
3	2	200	118	1000	0.118	

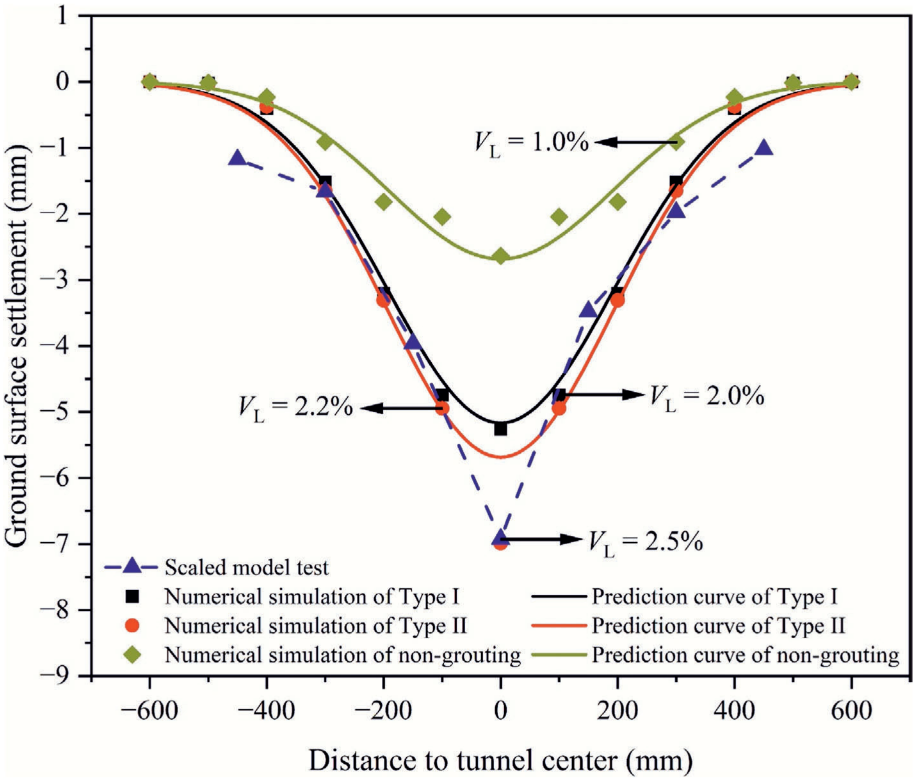

Fig. 7. GSS at $\alpha_{GVR} = 200\%$: comparison between numerical simulations and predicted results.

medium, the coarse-grained strata exhibit pronounced heterogeneity, discreteness, and high permeability, with structural stability mainly dependent on interparticle friction and interlocking. During the grouting process, continuous infiltration and disturbance of the grout may reduce the frictional resistance at particle contacts, which disrupts the original force-chain network of the soil skeleton and impedes the formation of potential self-stabilizing structures (such as soil arches). Consequently, the macroscopic mechanical properties of the soil deteriorate, resulting in anomalously high GSS values. A quantitative analysis of the granular microstructure is presented in Section 4.2.

Figure 8 illustrates grout spreading modes under different grouting-opening distribution configurations. The results demonstrate significant differences in spreading patterns between the Type I and Type II models. At low GVR, grout propagated in a semi-circular pattern in both models, with a gravity-induced downward offset the center. The semi-circular spread pattern is highly consistent with the grout spread modes reported by Ye et al. (2019) and C. Liu et al. (2024a), demonstrating good applicability of the model in simulating grout spread behavior. As GVR increased, the spreading radius progressively expanded, enabling grout to fill the tail void and intersect with material from adjacent openings. However, although increasing GVR enhanced spreading and intersection, grout in the Type I model faced substantial upward resistance due to sudden soil collapse at the tunnel crown and gravitational effects. Consequently, even at high GVR, grout in the Type I model did not reach the tunnel crown. This phenomenon is consistent with the findings of C. Liu et al. (2024b) in scaled four-opening synchronous grouting tests, confirming the limited effectiveness of Type I configurations for crown grouting. In contrast, the Type II model demonstrated improved grout filling at crown and bottom voids. Notably, the numerical simulations focused on the brief synchronous grouting phase, and non-grouted regions can be subsequently filled via gravity-driven permeation over time.

An unstable grout pressure was observed in the numerical simulation, consistent with the findings reported by Ding et al. (2019) through model tests and by C. Liu et al. (2024a) via numerical simulations. The instability of grout pressure at a given location primarily results from the interaction between two competing mechanisms: continuous grout injection increases local pressure, whereas spread dissipates it. These opposing processes lead to fluctuations in grout pressure. Note that numerical simulation accuracy and sensor precision in model tests may have also contributed to the observed fluctuations. Further, certain differences are noted between the numerical model and scaled model test used in this study (six-port vs. four-port grouting conditions), and the available experimental data were limited. Moreover, most existing analytical solutions for grout pressure distribution are based on filling spread in soft soils. Analytical models applicable to permeation spread in coarse-grained strata remain underdeveloped. Therefore, direct validation of grout pressure is not achievable. Because grout pressure was not the major focus of

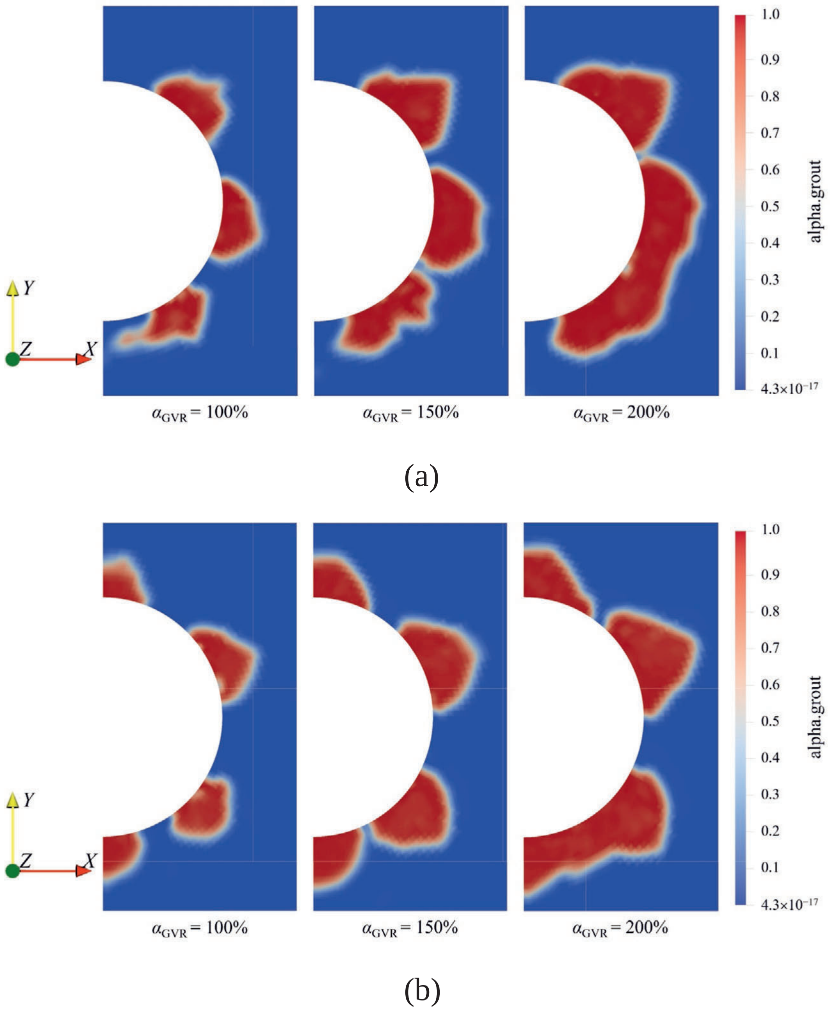

Fig. 8. Grout spreading modes at different GVRs. (a) Type I, and (b) Type II.

this study, a systematic analysis was not conducted within the present research framework.

4 Results and discussions

4.1 Macroscopic responses during synchronous grouting

4.1.1 Soil displacement

The evolution of the particle velocity field of the soil surrounding the tunnel is illustrated in Figs. 9 and 10. The results indicate that after the shield shell boundary was removed, the surrounding soil was rapidly displaced toward the tunnel (at 0.01 s). At approximately 0.05 s, the soil above the tunnel reached the crown, and further downward movement was constrained by the tunnel lining. Owing to the relatively flat geometry at the tunnel crown, particles in this region remained relatively stable during the initial phase, whereas the soil located farther above continued to settle. By 0.09 s, the tail-void above the tunnel center was fully filled with soil, and some particles began migrating downward along the right tunnel edge, continuing to fill the lower tail void. These movement paths are indicated by arrows in Fig. 9. The particle trajectories had a significant influence on the vertical stress distribution of the soil under non-grouting conditions, as discussed in Section 4.1.2. The evolution of particle displacement can be divided into two distinct phases. The first phase involved the rapid filling of the tail-void above the tunnel center, completed within approximately 0.09 s. During this phase, the particle displacement patterns were similar under different conditions. The second phase was characterized by a gradual downward migration of particles along the right tunnel edge, slowly filling the lower tail void. Differences between grouting and non-grouting conditions became apparent primarily during the second phase. Under non-grouting conditions, the soil reached a stable state shortly after 0.75 s. By 1.50 s, particles became stationary, and the tail-void was almost entirely filled, except for localized areas at the tunnel invert. Under grouting conditions, as grouting continued, the soil adjacent to the grouting openings around the tunnel haunch became unstable under grout pressure, causing particles to migrate toward the bottom and gradually fill the voids. When GVR reached 50% (at 0.75 s), the tail-void was mostly filled with particles and

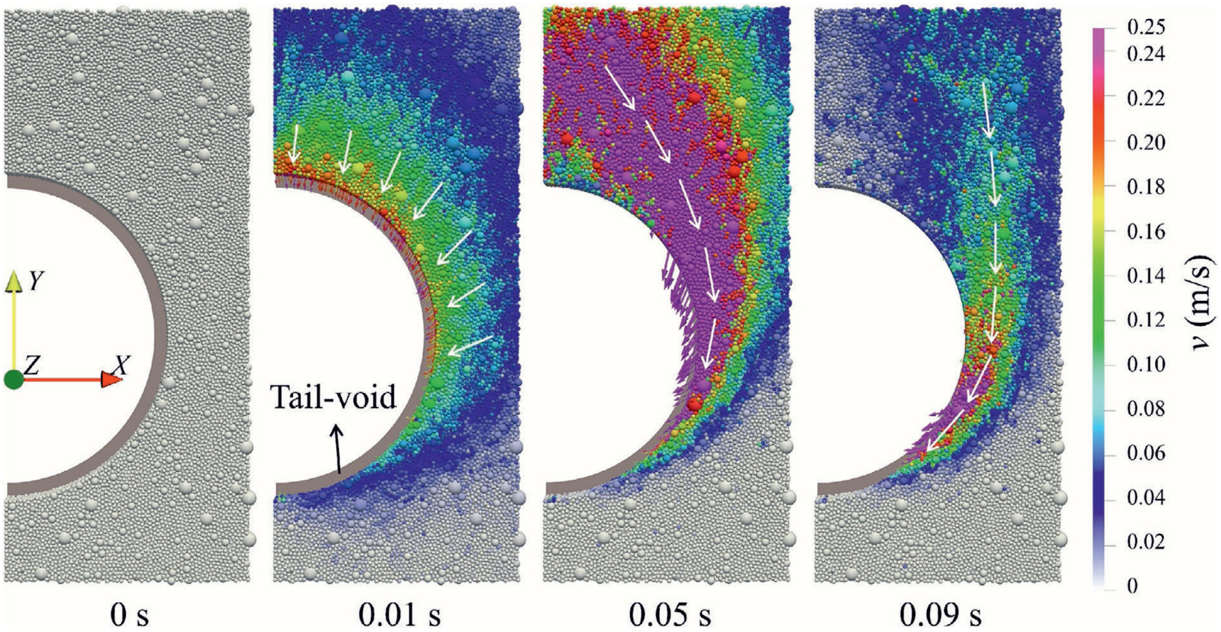

Fig. 9. Velocity field of particles in the first 0.09 s after the shield machine passes.

grout, while the soil above the tunnel continued to deform. The evolution of the velocity field revealed that grout from the grouting openings above the tunnel center can only spread by permeation, as the soil collapse rate significantly exceeded the grout spreading rate, resulting in rapid occupation of the voids by falling soil before the grout could adequately fill them. Consequently, only permeation spread occurred. In contrast, grout from those under the tunnel center exhibited a composite filling-permeation spreading mode. Notably, with increasing GVR, the unstable soil region at the tunnel crown in the Type II model was significantly larger than that in the Type I model because of continuous grouting from the top grouting opening. This indicates a more pronounced impact on GSS in the central tunnel region. Furthermore, the distribution of the particle velocity field closely aligns with the grout spread paths, suggesting a direct correlation between soil particle instability and the disturbances induced by grout permeation, which in turn influences the development trend of GSS.

Numerical simulations revealed significant differences in the morphological characteristics of surface settlement troughs under distinct grouting-opening distribution modes (Fig. 11), with the non-grouting condition ($\alpha_{\mathrm{GVR}} = 0$) serving as the benchmark for comparative analysis. The GSS values in the Type I model exhibited reduced variability within $0.25D$ of the tunnel center and were markedly lower than those in the Type II model. The overall GSS at the tunnel center of the Type I configuration was reduced by 1.76 mm (25%) compared to the six-opening Type II configuration. The disparity gradually diminished with distance from the center. This trend is attributed to the stronger influence of crown grouting openings in the Type II model on overlying soil near the tunnel center compared with the Type I configuration, resulting in significantly higher GSS magnitudes at the center. Additionally, a notable GSS disparity was observed between grouting and non-grouting conditions arising from the natural soil response in the latter, where grout absence enabled post-collapse arching effects, yielding substantially smaller short-term GSS than in the grouted scenarios. These mechanisms, further discussed in Section 4.2, underscore the critical role of grouting-opening distribution in ground settlement dynamics. Although this result may seem counterintuitive, existing research suggests that the mechanism by which synchronous grouting affects GSS in coarse-grained strata differs from that in homogeneous soils, such as soft clay. For example, Liu et al. (2024a) found through scaled model tests that GSS increases with GVR. Similarly, Rong et al. (2022) noted that coarse-grained strata exhibit significant heterogeneity and discontinuity, resulting in large fluctuations in settlement induced by shield tunneling, which makes prediction more challenging. Moreover, construction data revealed no direct correlation between GSS and GVR in coarse-grained strata. Although GVR is theoretically an important parameter influencing GSS, existing studies indicate that its role in coarse-grained strata deviates significantly from conventional expectations.

Figure 12 illustrates the variation of maximum GSS with time under different grouting conditions. The maximum GSS increased progressively over time. Despite increasing GVR during this period, which enhanced soil support and inhibited GSS development, the high permeability and heterogeneity of the sandy cobble stratum sustained continuous soil-grout interaction during grout

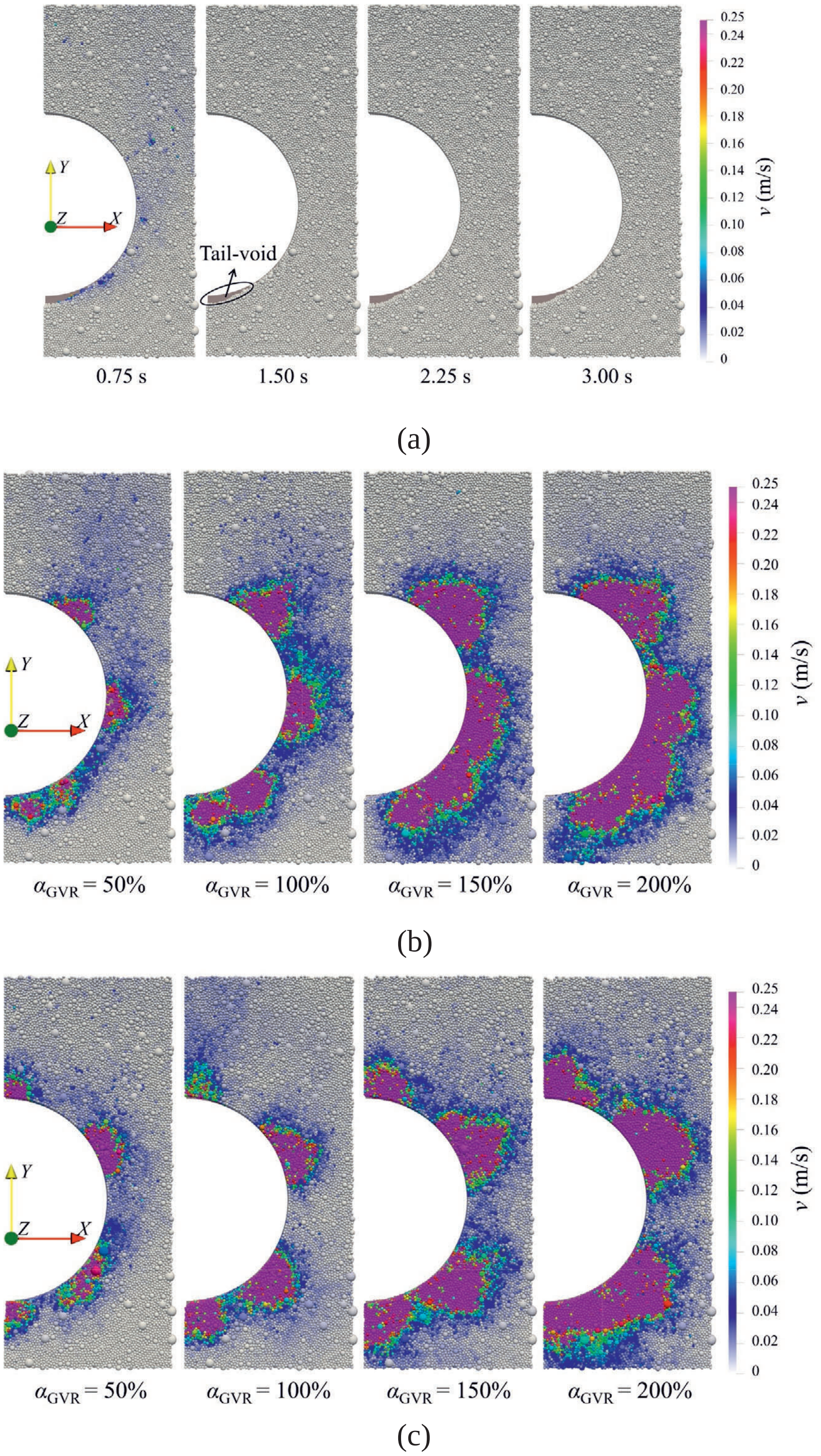

Fig. 10. Velocity field development of particles. (a) Non-grouting case, (b) Type I, and (c) Type II.

permeation. This interaction induced soil particle displacement, causing structural damage and cumulative deformation that elevated GSS. The result demonstrates that grouting duration dominates GSS evolution in sandy cobble strata. Before 0.33 s ($\alpha_{\mathrm{GVR}} = 22\%$), GSS under non-grouting conditions exceeded grouting scenarios. However, between 0.33 and 0.61 s ($\alpha_{\mathrm{GVR}} = 41\%$), grouting-induced GSS gradually surpassed non-grouting

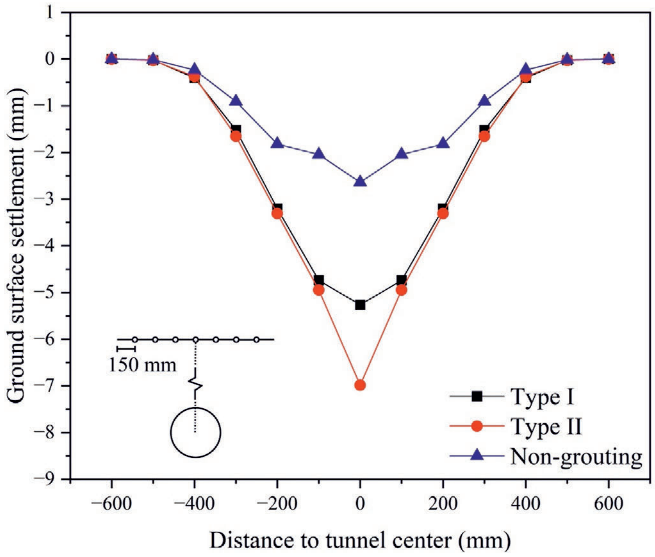

Fig. 11. GSS distributions in different grouting conditions at 3 s ($\alpha_{\mathrm{GVR}} = 200\%$).

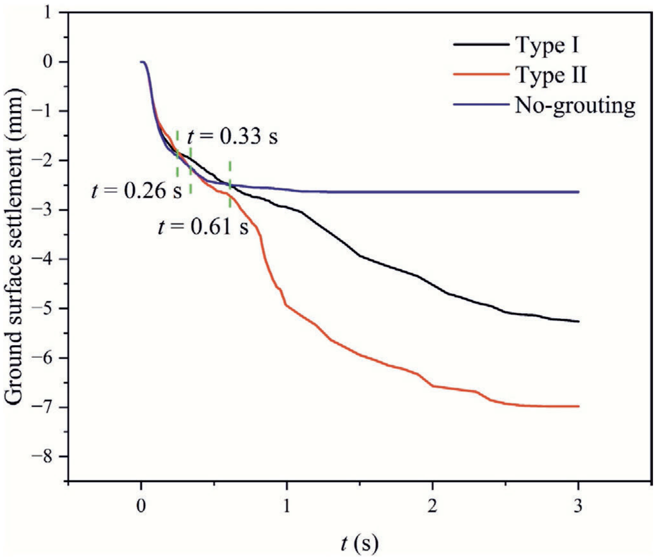

Fig. 12. Development of maximum GSS over time under different grouting conditions.

values, indicating that synchronous grouting initially suppresses but later exacerbates GSS owing to prolonged grout permeation-induced soil structural changes. Notably, maximum GSS stabilized approximately at 1.5 s under non-grouting conditions, whereas grouting conditions caused continuous GSS growth in the presence of persistent grouting disturbances. Furthermore, prior to 0.26 s ($\alpha_{\mathrm{GVR}} = 17\%$), the GSS in the Type I model exceeded that in the Type II model, highlighting the early-stage stabilizing effect of grouting pressure on crown-adjacent soil.

4.1.2 Stress in surrounding soil

The understanding of soil response is primarily founded on the theoretical framework of continuum mechanics. To establish an effective link between the discrete and continuous parameters, particle-scale measurements must be converted into the properties of continuum mechanics. For this purpose, Christoffersen et al. (1981) proposed a definition of the stress tensor for granular materials:

$$\sigma_{ij} = \frac{1}{V} \sum_{N_c} f_i^{\mathrm{c}} l_j^{\mathrm{c}}, \tag{18}$$

where V is the total volume of the computational unit; N_{c} is the total number of contacts; f_i^{c} is the contact force; and l_j^{c} is the branch vector connecting the centers of the two contacting particles.

Figure 13 illustrates the vertical stress evolution of soil during the initial 0.03 s. In the numerical simulations, particles were randomly generated above the model area and allowed to settle naturally under gravity until reaching a stable state, thereby realistically reproducing the formation process of the coarse-grained strata in the scaled model test. The significant frictional resistance and interlocking among sandy gravel particles led to micro-scale soil arching structures spontaneously forming in localized regions after stabilization. As a result of the soil arching effect, the stress transmission path was deflected, leading to local fluctuations in the vertical stress field that deviated from the linear increase predicted by classical continuum theory at $t = 0$ s. This phenomenon may also be influenced by the boundary conditions. However, the overall vertical stress still followed the fundamental trend of increase with depth. This discontinuous stress distribution reflects the inherent discrete nature of coarse-grained strata. Following shell-boundary removal, an elliptical stress-relief zone formed around the tunnel within 0.01 s, extending approximately to 0.5D below the tunnel invert and 1D above the tunnel crown. Within this zone, instantaneous stress release significantly reduced vertical stresses, reflecting localized support loss and stress redistribution. Over the 0.03 s period, stress redistribution propagated upward from the tunnel vicinity toward the ground surface, culminating in widespread stress reduction and soil structure loosening across the affected region.

Figure 14 illustrates the temporal variation of vertical soil stress under different grouting conditions. Soil stress evolution exhibited pronounced complexity owing to turbulent grout flow and unstable grout pressure. To improve visualization and highlight stress distribution trends, the stress contour range was constrained to 0–2000 Pa. Specifically, vertical stress values exceeding 2000 Pa are uniformly represented in red. As the grout-volume ratio (GVR, α_{GVR}) increased, vertical soil stress near the tunnel demonstrated a marked upward trend, attributed to greater grout injection volumes exerting stronger soil-compaction effects. This compaction is transmitted through interparticle contacts, ultimately elevating the vertical stress. At the simulation endpoint ($t = 3$ s), non-grouting conditions produced a wedge-shaped vertical stress distribution, correlating with horizontal distance from the tunnel center,

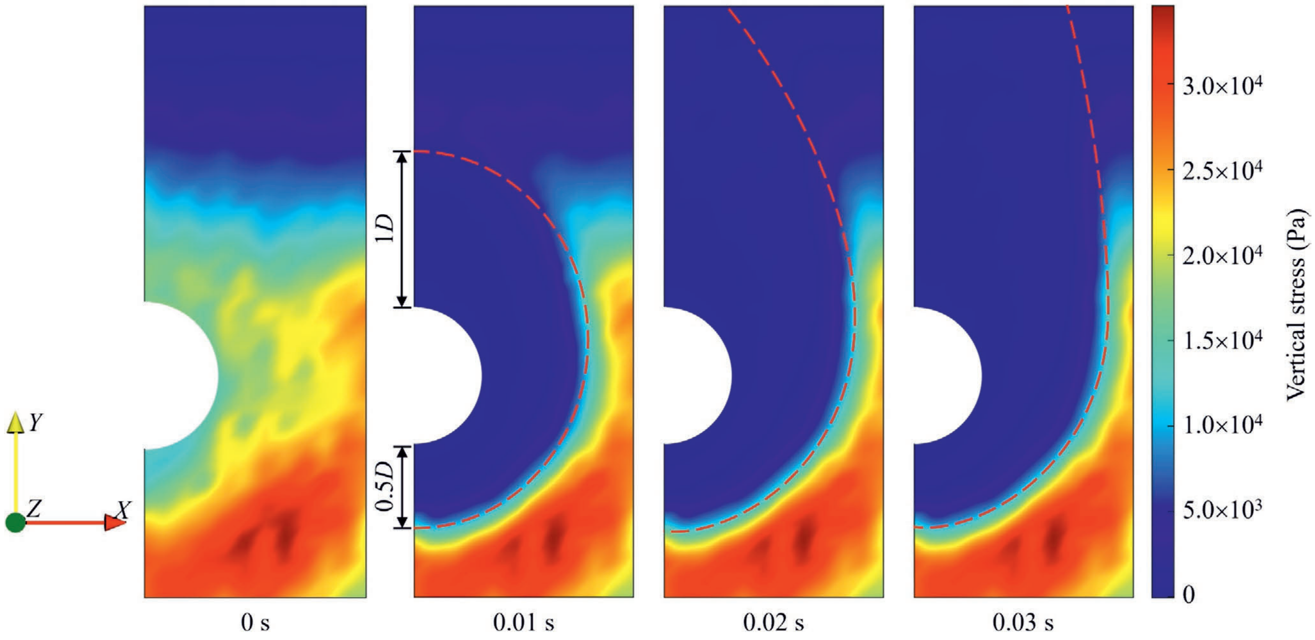

Fig. 13. Vertical stress development in soil during the initial 0.03 s. (Unit: Pa)

whereby stress decreased gradually, reaching a minimum approximately at 0.5D, then increased with further distance. The wedge-shaped vertical stress distribution exhibits a strong correlation with the particle velocity field at 0.09 s in Fig. 9, indicating that particle displacement played a dominant role in shaping the stress field. In contrast, vertical stress near the tunnel invert remained significantly lower owing to stress release post-shell removal. Natural soil collapse predominantly occurred above the tunnel center, leaving the invert tail-void minimally affected by displacement, thereby maintaining low invert stress. Higher vertical stress near the tunnel enhanced mechanical stability by improving load-bearing capacity for overlying strata. These findings underscore that the behavior of grout flow and GVR critically govern soil mechanical responses during sandy cobble stratum grouting.

4.2 Micro responses during the synchronous grouting

4.2.1 Normal contact between particles

Currently, micromechanical analysis methods based on particle contact fabric have been widely applied to study the behavior of granular materials (Bokkisa et al., 2023; Irani et al., 2024; Zhang et al., 2023). According to the macroscale soil behavior presented in Section 4.1, the primary effects of grouting occur in the region above the tunnel center. Therefore, the disturbed soil in this region was examined from a microscale perspective. Direct observation of force-chain evolution during synchronous grouting is challenging (C. Liu et al., 2024a). To address this limitation, rose diagrams representing the normal distribution of soil particle contacts were analyzed to investigate the soil arching effect and the influence of different grouting opening distribution modes on grouting-induced GSS. The analysis employed 10° statistical intervals, with spatial zones defined by stress distributions at the non-grouting simulation endpoint (as shown in Fig. 15(a)). Before grouting (Fig. 15(b)), dominant particle contact orientations aligned vertically upward, reflecting load transfer through vertical interparticle forces. Under non-grouting conditions (Fig. 15(c)), post-collapse soil arching formed with a centerline at 0.5D from the tunnel center, consistent with the particle trajectories shown in Fig. 9, where crown soil stabilized after tail-void infill, while ongoing edge-ward particle migration shifted the arch centerline toward tunnel peripheries.

In the grouting scenarios shown in Fig. 15(d) and (e), the soil-arching effect persisted but weakened, with centerlines shifting to 0.25D (Type I) and near-tunnel-center (Type II) positions. These shifts spatially correlate with uppermost grouting openings, indicating that grout-induced disturbance governed the soil-arch geometry. Grout injection disrupted particle contacts and force chains above the tunnel, attenuating natural arching and redistributing contact forces. This reconfiguration elevated GSS under grouting versus non-grouting conditions. Specifically, the offset grout openings in Type I induced asymmetric arch degradation, whereas the central top opening in Type II localized disturbance near the tunnel axis. Collectively, grouting modifies soil mechanical states by reorganizing force chain networks, directly linking particle-scale interactions (e.g., contact reorientation, arch weakening) to macroscale GSS trends in sandy cobble strata. It should be noted that this conclusion—GSS under non-grouting conditions is smaller than that observed under grouting conditions—applies only to the short term

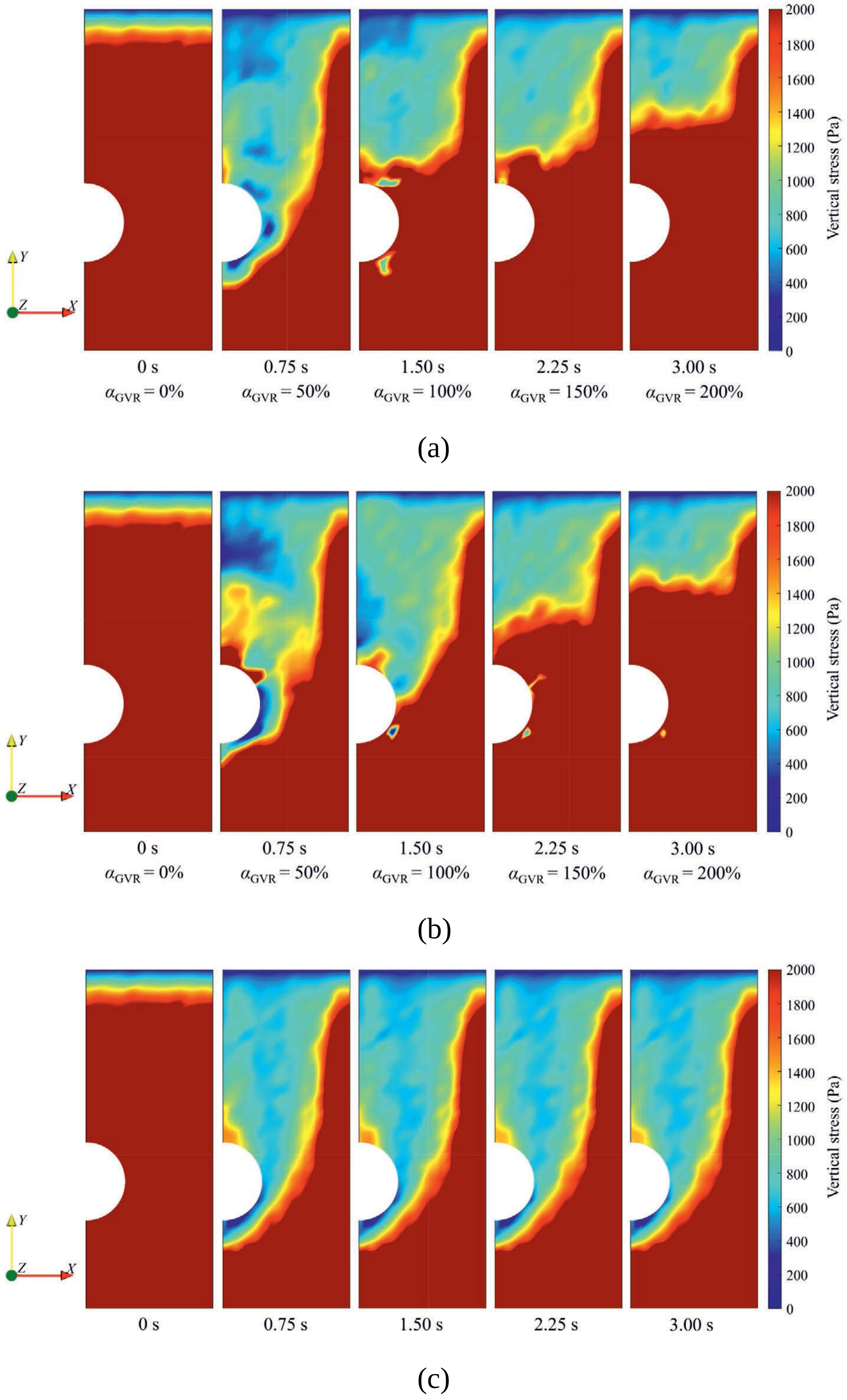

Fig. 14. Development of vertical soil stress with time. (a) Type I, (b) Type II, and (c) non-grouting case.

after grouting. Over a longer timescale, non-grouting condition may present a potential risk of increased GSS, as external disturbances can trigger more severe stratum deformations, potentially resulting in total settlement exceeding that under grouting conditions.

4.2.2 Coordination number

Section 4.1.1 revealed significant differences in GSS curves between grouting-opening distribution modes within 0.25D of the tunnel center. Settlement trough curves for grouting and non-grouting conditions also diverged

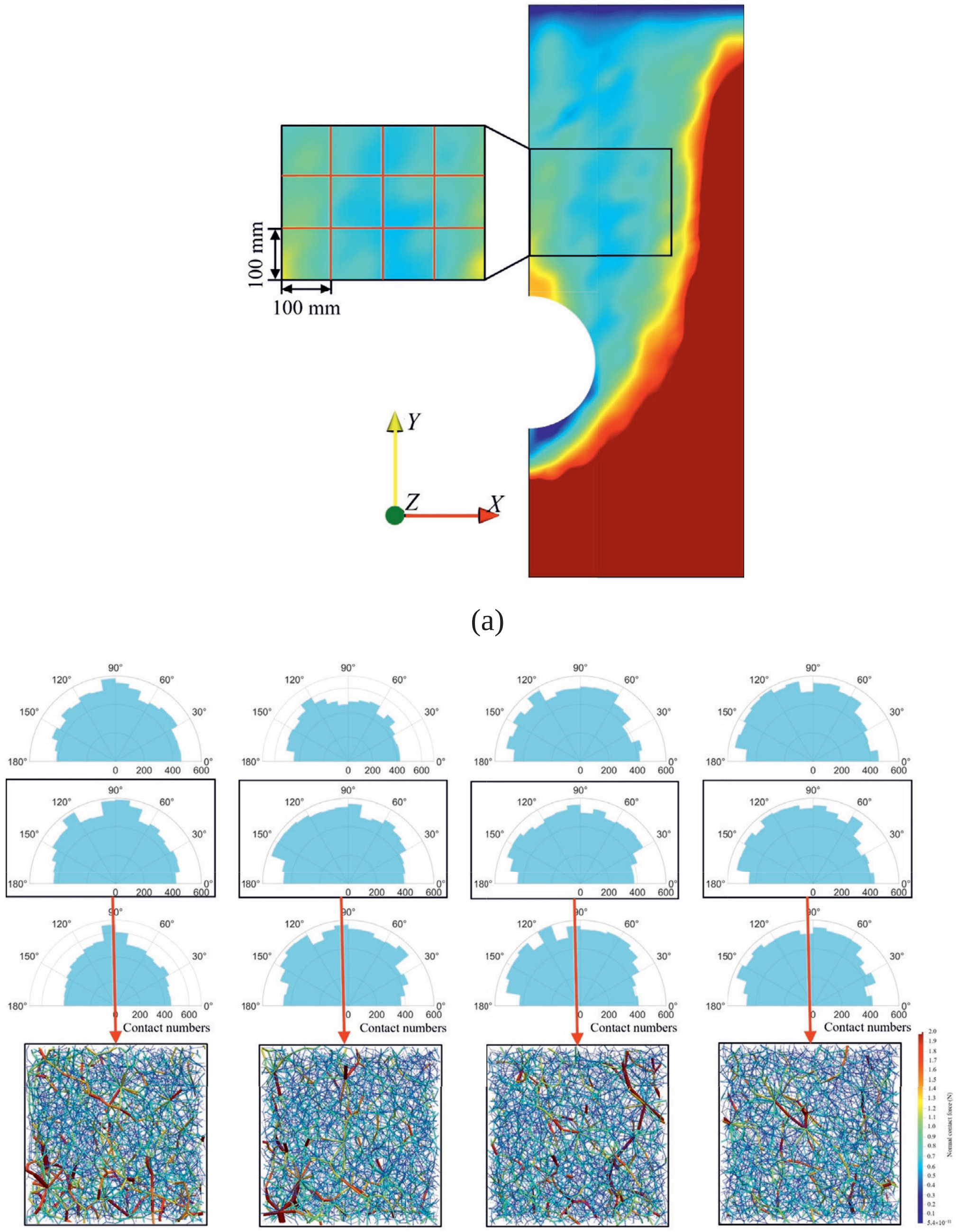

(a)

(b)

Fig. 15. Distributions of normal contact force. (a) Division of regions, (b) before grouting, (c) non-grouting, (d) Type I ($\alpha_{\mathrm{GVR}} = 200\%$), and (e) Type II ($\alpha_{\mathrm{GVR}} = 200\%$).

markedly within 1D of the tunnel. To identify the microstructural mechanisms underlying these macroscopic trends, a detailed microstructural analysis was performed on the four critical regions defined in Fig. 16(a).

Coordination number is a key metric for quantifying the contact number per particle in granular materials. It is regarded as the most fundamental and direct microscopic scalar parameter within a particle system. Thornton and Antony (2000) defined the mechanical coordination number (Z_{m}) by considering only active particles:

$$Z_{\mathrm{m}} = \frac{2N_{\mathrm{c}} - N_1}{N - N_0 - N_1}, \tag{19}$$

where N_{c} is the total number of contacts in the system; N is the total number of particles; N_0 is the number of particles with no contacts; and N_1 is the number of particles with one contact.

The evolution of Z_{m} during synchronous grouting is illustrated in Fig. 16. After the removal of the shell boundary, the soil above the tunnel center collapsed and was displaced toward the tunnel, altering particle contacts. This

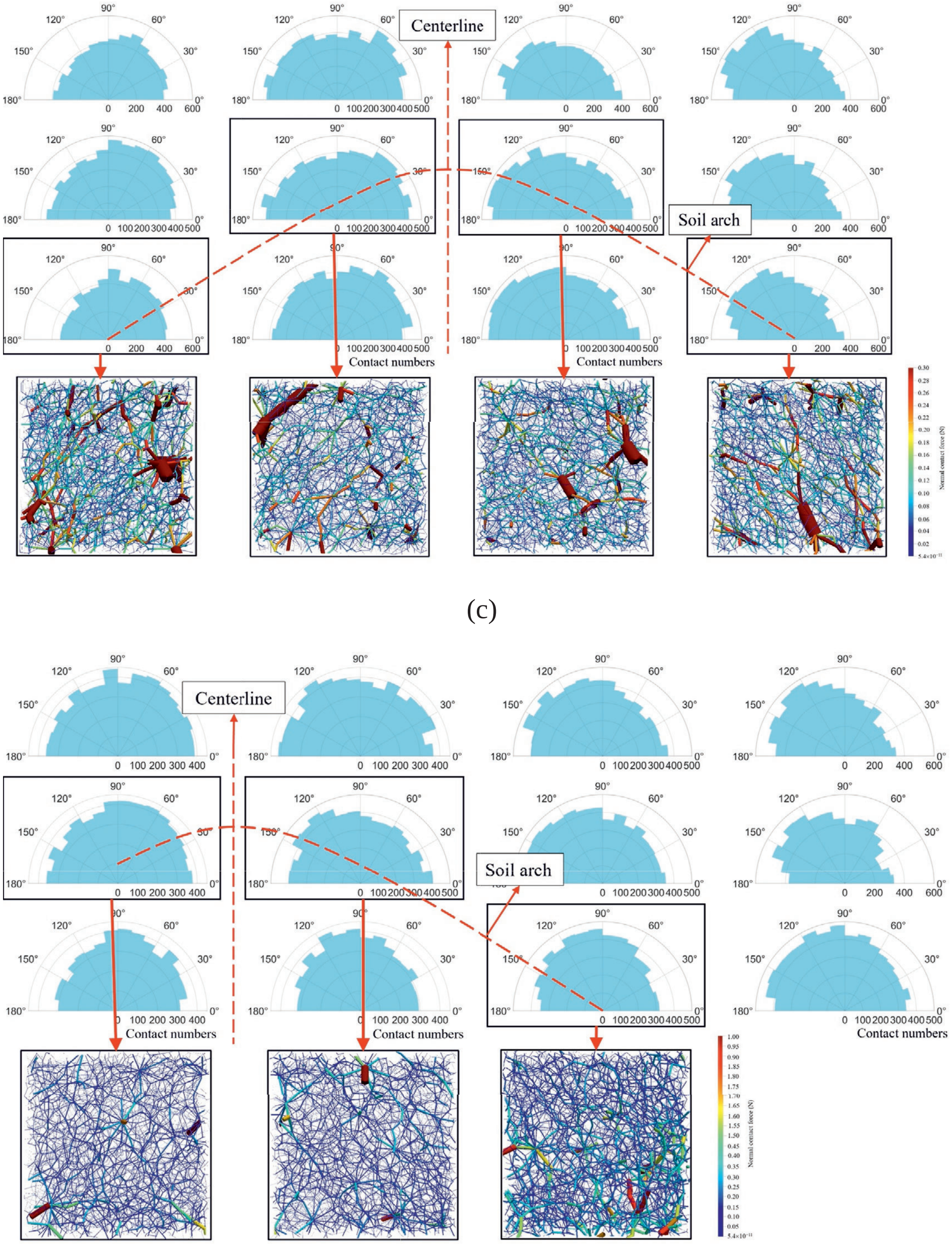

(c)

(d)

Fig 15. *(continued)*

process caused a loss of particle contacts, loosened the soil structure, and led to a significant reduction in Z_m values in the region above the tunnel center during the initial grouting stage. The rate of decline in Z_m diminished with increasing distance from the tunnel center, as shown in Fig. 16(b)–(e). Subsequently, as the soil was displaced toward the tunnel and filled the tail void, gradual compaction occurred, resulting in an increase in Z_m. However,

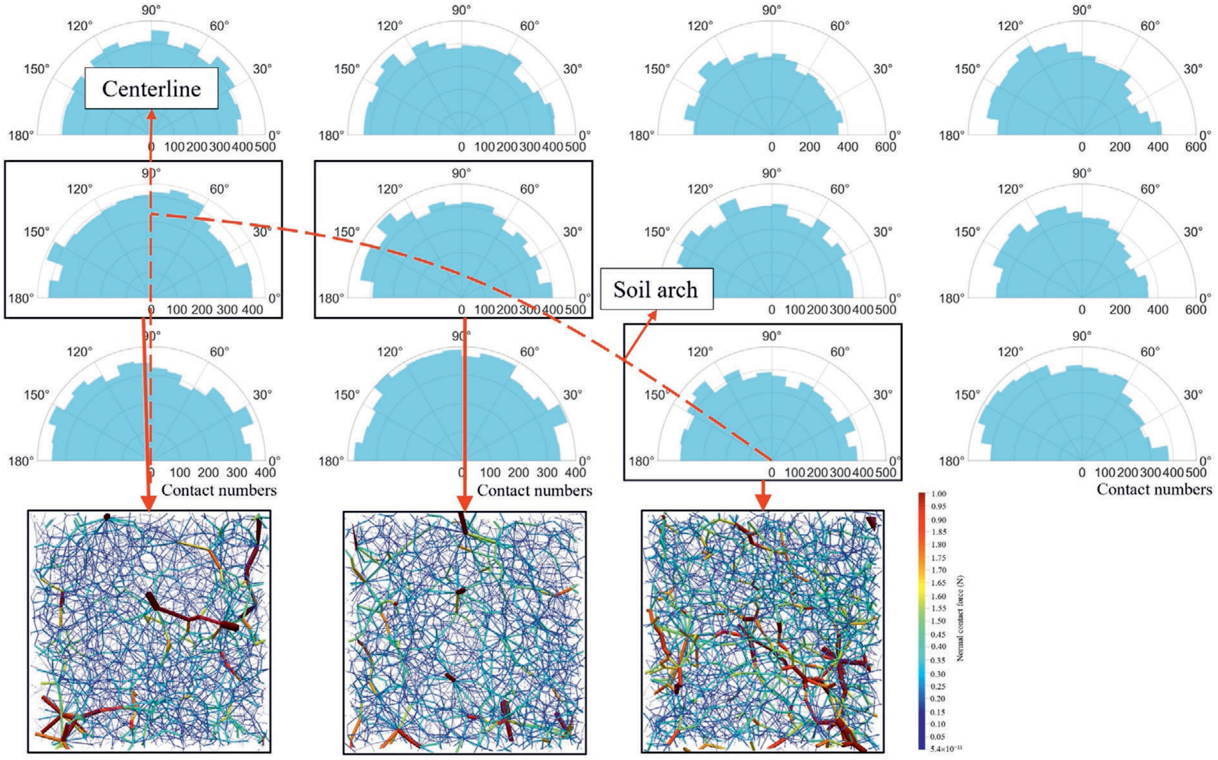

(e)

Fig 15. *(continued)*

even after gravitational compaction, the soil compactness remained substantially lower than in the pre-grouting state, with the final Z_m value reaching only approximately 85% of the initial value.

As depicted in Fig. 16, Z_m values under grouting conditions fluctuated marginally but remained markedly lower than those under non-grouting conditions. This discrepancy was most pronounced in regions I and II, where synchronous grouting continuously disturbed and compressed the soil above the tunnel center. The sustained grouting maintained soil particles in an unstable, high-stress state, reducing the mechanical coordination number. A lower Z_m reflected the tendency of the particle contact network to become sparser, thereby impairing the structural integrity of the force chain network. This microscopic alteration manifested macroscopically as a loosening and destabilization of the soil structure. Moreover, under grouting conditions, Z_m fluctuated without reaching stability, indicating that the soil above the tunnel remained unstable and was more likely to induce significant GSS, as shown in Figs. 11 and 12. In contrast, under non-grouting conditions, after the removal of the shield tail, soil particles naturally collapsed and accumulated to form a structure with a relatively high and stable Z_m (approximately 4.2). A high Z_m denotes a dense distribution of contact points among particles, which promotes the formation of a stable force chain network. This network enables efficient transmission of vertical loads through the soil arching structure, thereby inhibiting further development of GSS. The influence of grouting weakened progressively with distance from the tunnel center, as shown in Fig. 16 (b)–(e). Notably, grouting in the Type II model exerted a greater impact on soil deformation above the tunnel center, inducing pronounced Z_m fluctuations across regions. For example, Z_m values in region I remained lower for an extended duration under the Type II model compared to the Type I model. However, in other regions (i.e., regions II–IV), Z_m values showed no significant differences between grouting conditions.

4.2.3 Development of fabric anisotropy and contact orientation

The contact fabric of soil particles plays a pivotal role in determining the microscopic mechanical response of soil (Oda, 1972; Oda et al., 1985). Understanding microscopic variations in fabric is critical for analyzing grout–soil particle interactions. In this study, fabric anisotropy and its principal direction were employed to characterize the soil's fabric state. For simplicity, the analysis focused on contact information in the *x*-*y* plane, neglecting effects along the tunnel-axis direction (*z*-axis). Building on a simplified framework proposed by Xiong et al. (2021), the particle contact distribution function can be expressed as follows:

$$\bar{E}(\varphi) = \frac{[1 + \alpha\cos 2(\varphi - \beta)]}{2\pi}, \tag{20}$$

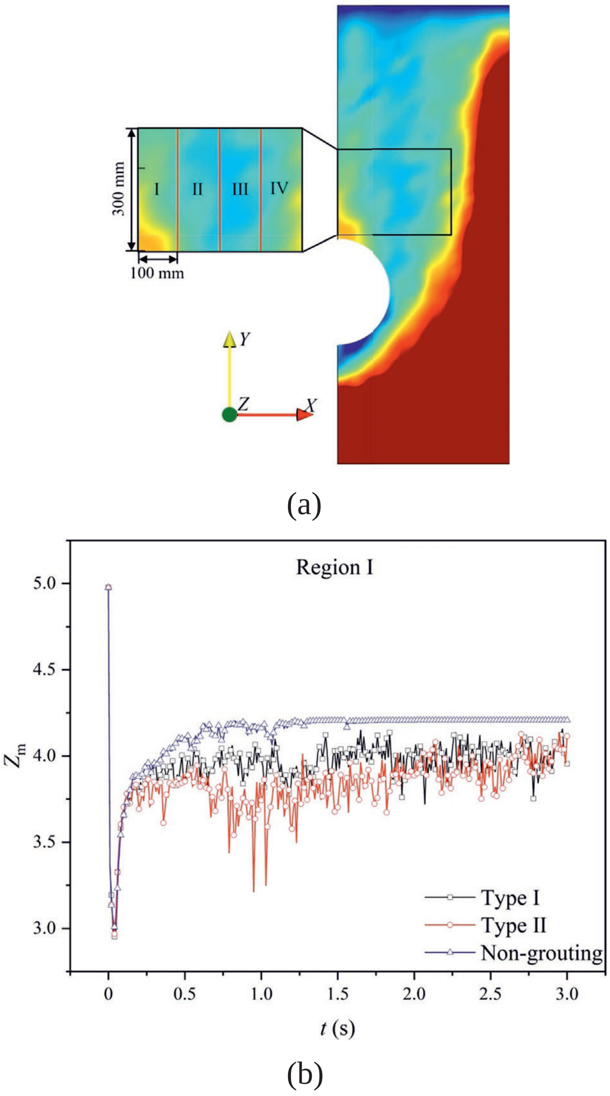

Fig. 16. Evolution of coordination number Z_m. (a) Division of regions, (b) region I, (c) region II (d) region III, and (e) region IV.

where φ is the inclination angle relative to the reference axis; $\bar{E}(\varphi)$ is the contact distribution function; and $\int_0^{2\pi} \bar{E}(\varphi)\mathrm{d}\varphi = 1$. The parameter α defines the magnitude of fabric anisotropy, and $\alpha = 0$ indicates an isotropic distribution. The parameter β is the principal direction of fabric anisotropy, which defines the angle between the principal direction of anisotropy and the positive x-axis (Xiong et al., 2021). The values of α and β are calculated as follows:

$$\alpha = 2\sqrt{\left[\int_0^{2\pi} \bar{E}(\varphi)\cos 2\varphi \mathrm{d}\varphi\right]^2 + \left[\int_0^{2\pi} \bar{E}(\varphi)\sin 2\varphi \mathrm{d}\varphi\right]^2}, \quad (21)$$

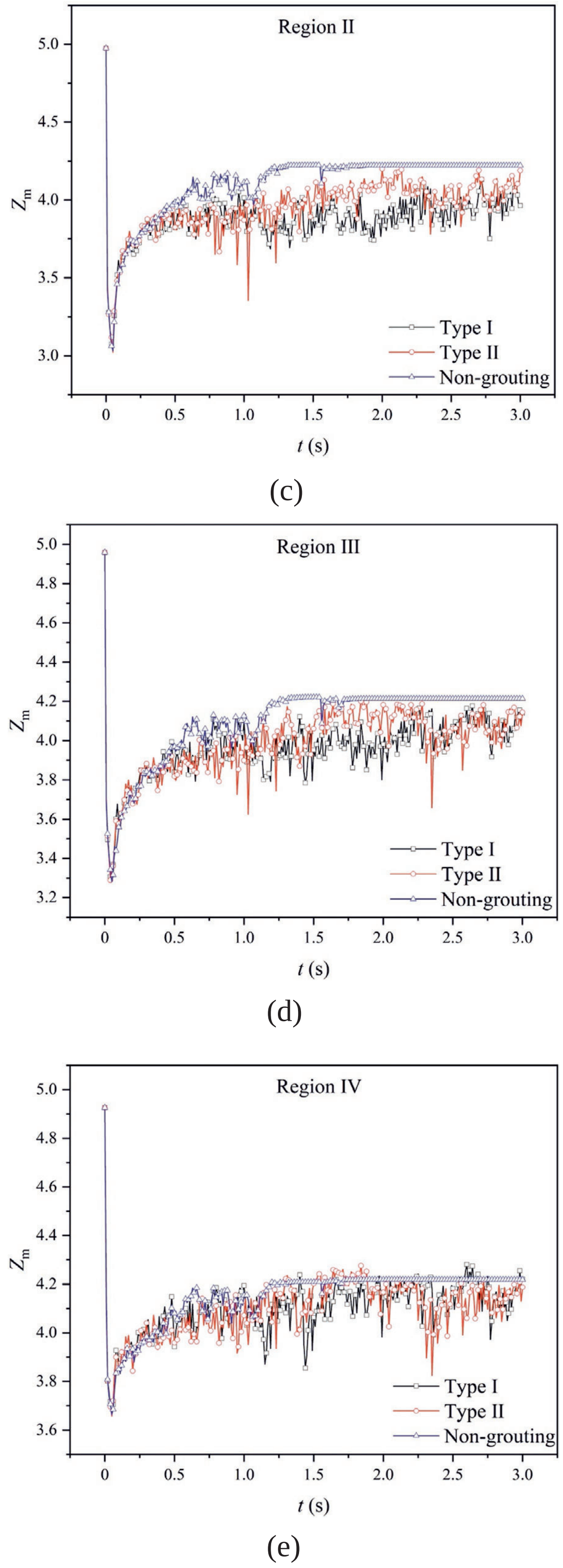

Fig 16. *(continued)*

$$\beta = \frac{1}{2}\arctan\frac{\int_0^{2\pi}\bar{E}(\varphi)\sin 2\varphi \mathrm{d}\varphi}{\int_0^{2\pi}\bar{E}(\varphi)\cos 2\varphi \mathrm{d}\varphi}. \tag{22}$$

The parameters α and β for the soil above the tunnel center are illustrated in Fig. 17. Prior to grouting, α values in all regions averaged approximately 0.13, whereas β was predominantly oriented upward (≈90°). As the distance from the tunnel center increased, β gradually rose. In Region I, β measured 87°, whereas in Regions II–IV, β averaged approximately 110°, suggesting a weak pre-grouting soil arching effect. Following shell boundary removal, significant α and β variations occurred across all regions. In Region I, both parameters initially decreased before increasing. In Region II, α and β first increased and then decreased. In Regions III and IV, α exhibited an initial increase followed by a decrease, whereas β continued to increase. These shifts resulted from rapid soil displacement toward the tunnel post-boundary removal. In the Type II model, the crown-located grouting opening exerted a stronger influence on Region I (Fig. 17(a)), enhancing soil isotropy and yielding lower α values relative to Type I. Under continuous injection, β in Type II stabilized near 90°, facilitating vertical load transfer. Without grouting, β stabilized at ≈65°, promoting soil arch development. In Region II (Fig. 17(b)), grouting maintained low α levels, whereas β fluctuated widely (0°–180°), reflecting marked soil displacement and isotropy. Without grouting, β progressively decreased and stabilized near 40°, further supporting arch formation. In Regions III and IV (Fig. 17(c) and (d)), sustained grouting reduced α, with β oscillations (120°–140°) enhancing arch formation. In Regions II–IV, α and β trends under both grouting modes aligned but diverged from the behavior in Region I, indicating that the influence of grouting opening configuration

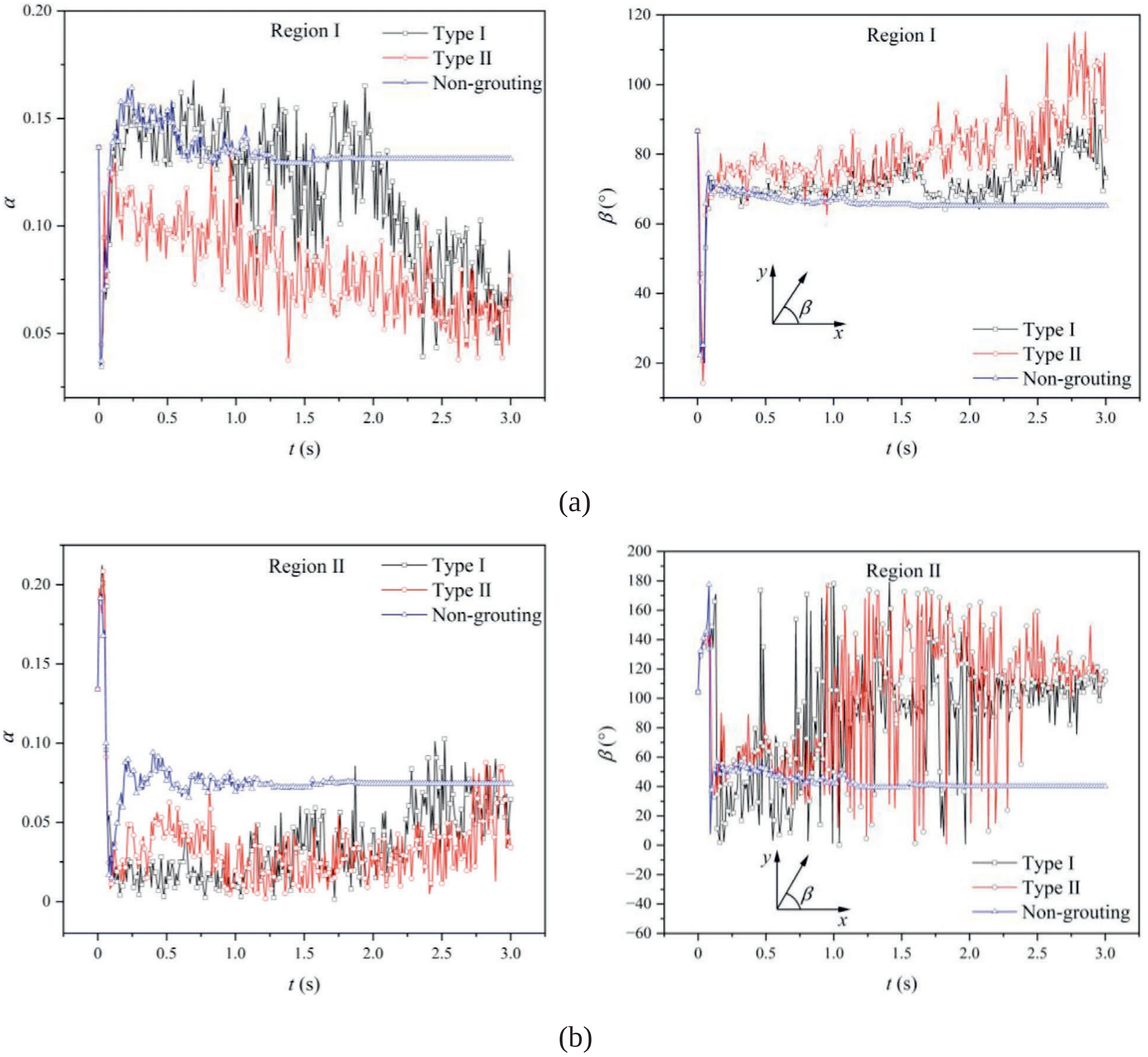

Fig. 17. Magnitude and principal direction of anisotropy (α and β) for soil fabrics: (a) region I, (b) region II, (c) region III, and (d) region IV.

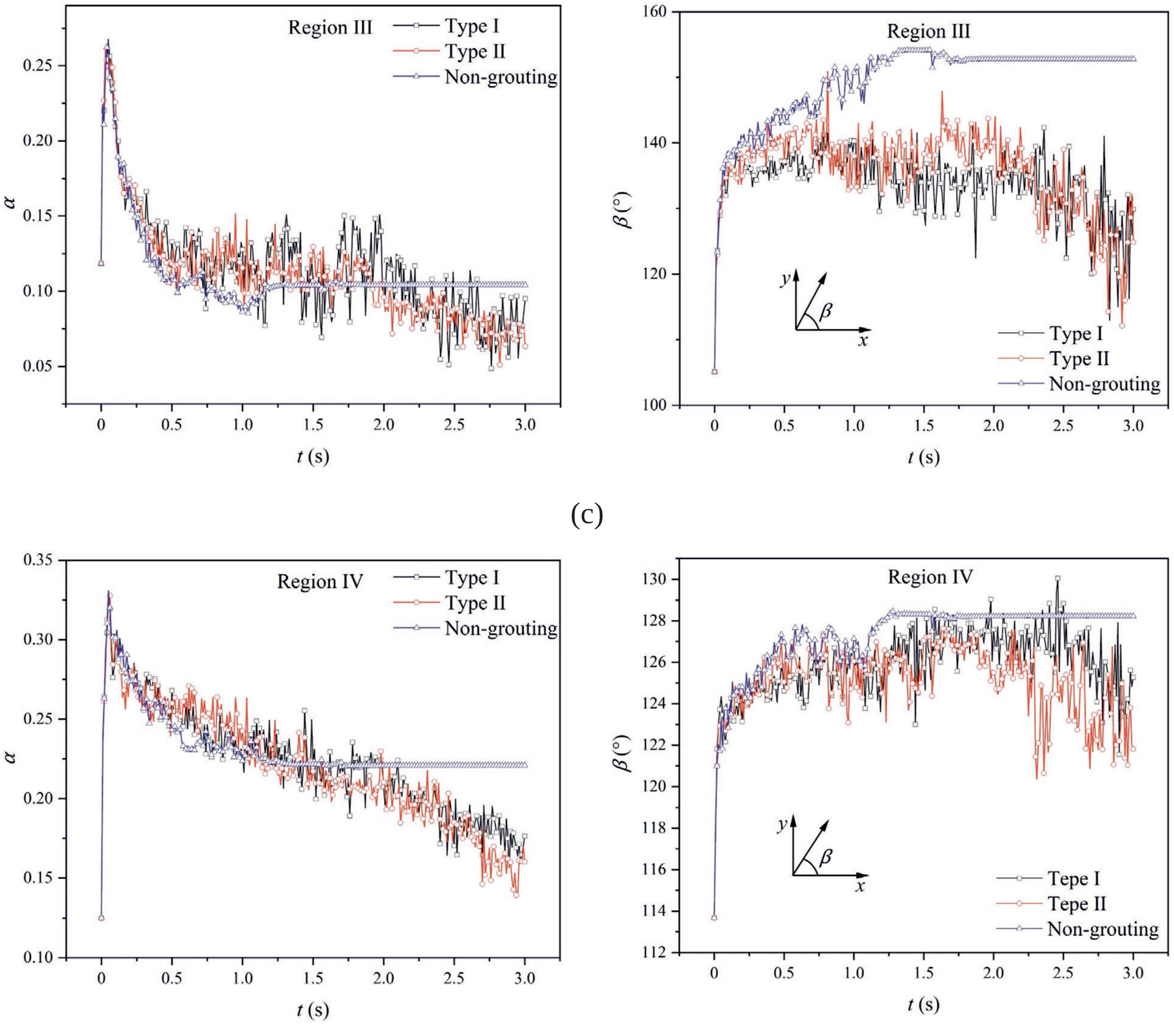

(c)

(d)

Fig 17. *(continued)*

was predominantly localized in Region I. Grouting impacts diminished with distance from the tunnel center, correlating with reduced α variability. Under non-grouting conditions, the overall α was greater than that under grouting conditions, particularly in Regions I and II. This indicates that the normal forces of particle contacts were more strongly aligned along a dominant direction, forming a directionally oriented force chain network. Unlike the fluctuating evolution of α and β during the grouting process, these parameters under non-grouting conditions tended to stabilize after a certain period, with their evolution closely following the variation of the Z_m. This stability suggested that the soil above the tunnel was in a relatively stable state. These behaviors collectively favor the formation of a soil arching structure, resulting in smaller GSS compared to grouting conditions.

The aforementioned analysis of the microscopic fabric of particle contacts under grouting and non-grouting conditions reveals the unique mechanical response mechanism of coarse-grained strata. Although grouting, after solidification of the grout, can ultimately enhance the overall stability of the strata, the dynamic disturbances during the grouting process alter the microscopic fabric of particle contacts, leading to an increase in GSS. This microscopic mechanism explains the greater GSS observed under grouting conditions in coarse-grained strata and further confirms the decisive influence of particle-scale microstructure on macroscopic mechanical behavior.

5 Conclusions

A numerical model of synchronous tail-grouting in coarse-grained ground was established using the coupled CFD–DEM method, focusing on two grouting opening configurations (Types I and II, both with six openings). The model was validated against existing experimental data. The influence of grouting opening configurations and presence of grouting was investigated from macroscopic and microscopic perspectives. This study elucidates the microscopic mechanisms of soil-grout interactions and explains the macroscopic phenomena observed during synchronous grouting. The findings provide a theoretical foundation for selecting shield machines with six grouting openings and for optimizing construction parameters for synchronous tail-grouting in coarse-grained ground. The key conclusions are summarized as follows:

(1) Grout propagation patterns: At low GVR, the grout spreads in a semicircular pattern, with the center slightly below the grouting opening owing to gravity. As GVR increased, grout from adjacent openings came into contact. Grout from upper tunnel openings propagated primarily via permeation, whereas lower openings exhibited a mixed filling-permeation mode. Type II configurations (with crown/invert openings) achieved significantly better grout coverage in the tunnel crown and invert compared to Type I.
(2) Grout-soil interaction and GSS: The crown-opening configuration (Type II) exerted greater influence, yielding GSS values within $0.25D$ of the tunnel center that were markedly higher than those of Type I. Under non-grouting conditions, natural soil collapse facilitates arching effects, resulting in substantially smaller short-term GSS compared to grouted cases. Soil disturbance duration was identified as the primary factor governing GSS in coarse-grained ground.
(3) Stress redistribution and arching behavior: Instantaneous stress redistribution occurred post-shield shell removal, forming an elliptical stress boundary that propagated toward the ground surface. Continuous grout injection increased circumferential soil stress. Under non-grouting conditions, vertical stress exhibited a wedge-shaped distribution, decreasing to a minimum at $0.5D$ from the tunnel center before rebounding with distance.
(4) Soil arch dynamics and fabric evolution: Under grouting conditions, the soil-arch centerline remained near the uppermost grouting opening, indicating a direct correlation between arch geometry and grouting-induced disturbance. Grout injection disrupted particle contacts and the force-chain networks above the tunnel center, weakening natural arching and redistributing interparticle contact forces.
(5) Spatial variability of grouting effects: Grouting opening configuration impacts were concentrated within $0.25D$ from the tunnel center horizontally. In both configurations, soil between $0.25D$ and $0.5D$ exhibited heightened sensitivity to grouting, with fabric anisotropy (α) remaining low and principal direction (β) oscillating sharply between 0° and 180°, reflecting pronounced displacement and isotropy.

Data availability

The data that support the findings of this study are available from the corresponding author upon reasonable request.

CRediT authorship contribution statement

Chao Liu: Writing – review & editing, Writing – original draft, Investigation, Funding acquisition, Formal analysis, Conceptualization. **Wei Chen:** Writing – review & editing, Visualization, Software, Formal analysis. **Delin Zhu:** Writing – review & editing, Software, Resources, Methodology. **Junzuo He:** Writing – review & editing, Validation. **Jie Cui:** Writing – review & editing, Supervision. **Xin Huang:** Writing – review & editing, Resources.

Declaration of competing interest

The authors declare that they have no known competing financial interests or personal relationships that could have appeared to influence the work reported in this paper.

Acknowledgement

The research was conducted with funding provided by the National Natural Science Foundation of China (Grant Nos. 52020105002 and 52178385) and the Natural Science Foundation of Guangdong Province (Grant No. 2024B1515040017).

References

Anderson, T. B., & Jackson, R. (1967). Fluid mechanical description of fluidized beds. Equations of motion. *Industrial & Engineering Chemistry Fundamentals, 6*(4), 527–539.

Bokkisa, S. V., Macedo, J., & Petalas, A. L. (2023). Fabric anisotropy effects on static liquefaction under constant shear drained loading. *Computers and Geotechnics, 163*, 105724.

Burns, S., Piiroinen, P., & Hanley, K. (2019). Critical time step for DEM simulations of dynamic systems using a Hertzian contact model. *International Journal for Numerical Methods in Engineering, 119*(5), 432–451.

Christoffersen, J., Mehrabadi, M. M., & Nemat-Nasser, S. (1981). A micromechanical description of granular material behavior. *Journal of Applied Mechanics, 48*(2), 339–344.

Cundall, P. A., & Strack, O. D. L. (1979). A discrete numerical model for granular assemblies. *Geotechnique, 29*(1), 47–65.

Ding, W. Q., Duan, C., Zhu, Y. H., Zhao, T. C., Huang, D. Z., & Li, P. N. (2019). The behavior of synchronous grouting in a quasi-rectangular shield tunnel based on a large visualized model test. *Tunnelling and Underground Space Technology, 83*, 409–424.

Goniva, C., Kloss, C., Deen, N. G., Kuipers, J. A. M., & Pirker, S. (2012). Influence of rolling friction on single spout fluidized bed simulation. *Particuology, 10*(5), 582–591.

Irani, N., Salimi, M., Golestaneh, P., Tafili, M., Wichtmann, T., & Lederer, J. (2024). Deep learning-based analysis of true triaxial DEM simulations: Role of fabric and particle aspect ratio. *Computers and Geotechnics, 173*, 106529.

Kasper, T., & Meschke, G. (2006). A numerical study of the effect of soil and grout material properties and cover depth in shield tunnelling. *Computers and Geotechnics, 33*(4/5), 234–247.

Kloss, C., Goniva, C., Hager, A., Amberger, S., & Pirker, S. (2012). Models, algorithms and validation for opensource DEM and CFD–DEM. *Progress in Computational Fluid Dynamics, an International Journal, 12*(2/3), 140–152.

Koch, D., & Hill, R. (2001). Inertial effects in suspension and porous-media flows. *Annual Review of Fluid Mechanics, 33*(1), 619–647.

Li, P. N., Ying, X., Shi, L., & Yu, D. H. (2021). Hydrodynamics analysis on fill diffusion in shield synchronous grouting based on CFD. *Chinese Journal of Underground Space and Engineering, 17*(S1), 126–132 (in Chinese).

Liang, X. M., Ying, K. C., Ye, F., Su, E. J., Xia, T. H., & Han, X. B. (2022). Selection of backfill grouting materials and ratios for shield tunnel considering stratum suitability. *Construction and Building Materials, 314*, 125431.

Liang, Y., Zhang, J., Lai, Z. S., Huang, Q. Y., & Huang, L. C. (2020). Temporal and spatial distribution of the grout pressure and its effects on lining segments during synchronous grouting in shield tunnelling. *European Journal of Environmental and Civil Engineering, 24*(1), 79–96.

Liu, C., Cui, J., Zhang, Z. X., Liu, H., Huang, X., & Zhang, C. Q. (2021a). The role of TBM asymmetric tail-grouting on surface settlement in coarse-grained soils of urban area: Field tests and FEA modelling. *Tunnelling and Underground Space Technology, 111*, 103857.

Liu, C., Zhu, D. L., Cui, J., Jing, L., & Huang, X. (2024a). Investigation on synchronous grouting process during shield tunneling in coarse grained ground using CFD-DEM approach. *Computers and Geotechnics, 170*, 106308.

Liu, C., Zhu, D. L., Liu, H., Cui, J., Zhang, X. Y., Rehman, M. U., & Huang, X. Y. (2024b). Influence of synchronous grouting on surrounding sandy cobbles during shield tunnelling process: Insights from a scaled model test. *Tunnelling and Underground Space Technology, 147*, 105728.

Liu, F. Z., Chen, W., Liu, C., Yang, Y. B., Wang, J., & Liu, Y. (2024c). The evolution of grouting pressure and ground deformation induced by synchronous grouting during shield tunneling in soft soil: An investigation based on scaled model test and CEL simulation. *Canadian Geotechnical Journal, 62*, 1–20.

Liu, J., Li, P. N., Shi, L., Fan, J., Kou, X. Y., & Huang, D. Z. (2021b). Spatial distribution model of the filling and diffusion pressure of synchronous grouting in a quasi-rectangular shield and its experimental verification. *Underground Space, 6*(6), 650–664.

Liu, X. L., Wang, F., Huang, J., Wang, S. J., Zhang, Z. Z., & Nawnit, K. (2019). Grout diffusion in silty fine sand stratum with high groundwater level for tunnel construction. *Tunnelling and Underground Space Technology, 93*, 103051.

Liu, X. X., Shen, S. L., Xu, Y. S., & Zhou, A. N. (2020). A diffusion model for backfill grout behind shield tunnel lining. *International Journal for Numerical and Analytical Methods in Geomechanics, 45*(4), 457–477.

O'reilly, M.P., & New, B.M. (1982). Settlements above tunnels in the United Kingdom—their magnitude and prediction (No. Monograph).

Oda, M. (1972). Initial fabrics and their relations to mechanical properties of granular material. *Soils and Foundations, 12*(1), 17–36.

Oda, M., Nasser, S. N., & Konishi, J. (1985). Stress-induced anisotropy in granular masses. *Soils and Foundations, 25*(3), 85–97.

Peck, R.B. (1969). Deep excavations and tunnelling in soft ground. *State of the Art Report, 7th International Conference on Soil Mechanics and Foundation Engineering*. (pp. 225–290).

Rong, X. N., Liu, X. D., Wen, Z., Lu, H., & Rong, X. L. (2022). Prediction of surface settlement induced by shield in sandy gravels stratum based on artificial neural networks. *Chinese Journal of Underground Space and Engineering, 18*(S2), 958–966 (in Chinese).

Ruan, W. J. (2005). Research on diffusion of grouting and basic properties of grouts. *Chinese Journal of Geotechnical Engineering, 27*(1), 69–73 (in Chinese).

Su, D., Yang, W. H., Lin, X. T., Zhang, X., Zhang, Z. Y., & Chen, X. S. (2024). Soil-carrying effect induced by super-large-diameter shallow-buried shield tunneling and treatment measures: A case study in Zhuhai, China. *Tunnelling and Underground Space Technology, 153*, 106037.

Thornton, C., & Antony, S. J. (2000). Quasi-static shear deformation of a soft particle system. *Powder Technology, 109*(1/2/3), 179–191.

Todaro, C., & Pace, F. (2022). Elastic properties of two-component grouts at short curing times: The role of bentonite. *Tunnelling and Underground Space Technology, 130*, 104756.

Vångö, M., Pirker, S., & Lichtenegger, T. (2018). Unresolved CFD–DEM modeling of multiphase flow in densely packed particle beds. *Applied Mathematical Modelling, 56*, 501–516.

Wang, S. M., He, C., Nie, L., & Zhang, G. C. (2019). Study on the long-term performance of cement-sodium silicate grout and its impact on segment lining structure in synchronous backfill grouting of shield tunnels. *Tunnelling and Underground Space Technology, 92*, 103015.

Wang, S. M., Lin, Z. Y., Peng, X. Y., Wang, X. M., Tu, G., & Song, Z. H. (2022). Research and evaluation on Water-dispersion resistance of synchronous grouting slurry in shield tunnel. *Tunnelling and Underground Space Technology, 129*, 104679.

Xiong, H., Yin, Z. Y., Zhao, J. D., & Yang, Y. (2021). Investigating the effect of flow direction on suffusion and its impacts on gap-graded granular soils. *Acta Geotechnica, 16*(2), 399–419.

Yan, B., Wang, R., Ding, B. S., Dai, F., & Wang, Y. (2024). Numerical simulation analysis of tunnel backfill grout based on DEM-FDM coupling and particle inlet. *Underground Space, 14*, 285–299.

Ye, F., Wang, B., Han, X., Liang, X., Ying, K. C., & Liang, X. M. (2020). Review of shield tunnel backfill grouting tests and its diffusion mechanism. *China Journal of Highway and Transport, 33*(12), 92–104 (in Chinese).

Ye, F., Yang, T., Mao, J. H., Qin, X. Z., & Zhao, R. L. (2019). Half-spherical surface diffusion model of shield tunnel back-fill grouting based on infiltration effect. *Tunnelling and Underground Space Technology, 83*, 274–281.

Zeng, Y., Njock, P. G. A., Xiong, W., Zhang, X. L., & Shen, S. L. (2023). Risks analysis of large diameter slurry shield tunneling in urban area. *Underground Space, 13*, 281–300.

Zhang, A., Jiang, M., & Wang, D. (2023). Effect of fabric anisotropy on the cyclic liquefaction of sands: Insight from DEM simulations. *Computers and Geotechnics, 155*, 105188.

Zhang, D. M., Ye, Z. W., Zhang, J. Z., Li, J. P., & Jia, J. W. (2022a). Influence of grouting on rehabilitation of an over-deformed shield tunnel lining in spatially variable soil. *Computers and Geotechnics, 152*, 104999.

Zhang, S. S., Dai, Z. R., & Bai, Y. (2015). Model test research on distribution law of grout pressure for simultaneous backfill grouting during shield tunneling. *China Railway Science, 36*(5), 43–53 (in Chinese).

Zhang, W. J., Qi, J. B., Zhang, G. L., Niu, R. J., Zhang, C., He, L. C., & Lyu, J. R. (2022b). Full-scale experimental study on failure characteristics of the key segment in shield tunnel with super-large cross-section. *Tunnelling and Underground Space Technology, 129*, 104671.

Zhao, T. C., Ding, W. Q., Qiao, Y. F., & Duan, C. (2019). A large-scale synchronous grouting test for a quasi-rectangular shield tunnel: Observation, analysis and interpretation. *Tunnelling and Underground Space Technology, 91*, 103018.

Zhu, H. P., Zhou, Z. Y., Yang, R. Y., & Yu, A. B. (2007). Discrete particle simulation of particulate systems: Theoretical developments. *Chemical Engineering Science, 62*(13), 3378–3396.

Zou, J. F., & Zuo, S. Q. (2017). Similarity solution for the synchronous grouting of shield tunnel under the vertical non-axisymmetric displacement boundary condition. *Advances in Applied Mathematics and Mechanics, 9*(1), 205–232.